



**HAL**  
open science

## **A Multimodel Investigation of Asian Summer Monsoon UTLS Transport Over the Western Pacific**

Laura L. Pan, Douglas Kinnison, Qing Liang, Mian Chin, Michelle L. Santee,  
Johannes Flemming, Warren P. Smith, Shawn B. Honomichl, James F.  
Bresch, Leslie R. Lait, et al.

► **To cite this version:**

Laura L. Pan, Douglas Kinnison, Qing Liang, Mian Chin, Michelle L. Santee, et al.. A Multimodel Investigation of Asian Summer Monsoon UTLS Transport Over the Western Pacific. *Journal of Geophysical Research: Atmospheres*, 2022, 127 (24), pp.e2022JD037511. 10.1029/2022JD037511 . insu-03897762

**HAL Id: insu-03897762**

**<https://insu.hal.science/insu-03897762v1>**






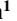












Submitted on 11 May 2023

**HAL** is a multi-disciplinary open access archive for the deposit and dissemination of scientific research documents, whether they are published or not. The documents may come from teaching and research institutions in France or abroad, or from public or private research centers.

L'archive ouverte pluridisciplinaire **HAL**, est destinée au dépôt et à la diffusion de documents scientifiques de niveau recherche, publiés ou non, émanant des établissements d'enseignement et de recherche français ou étrangers, des laboratoires publics ou privés.

Copyright

## A Multimodel Investigation of Asian Summer Monsoon UTLS Transport Over the Western Pacific

Laura L. Pan<sup>1</sup> , Douglas Kinnison<sup>1</sup> , Qing Liang<sup>2</sup> , Mian Chin<sup>2</sup> , Michelle L. Santee<sup>3</sup> , Johannes Flemming<sup>4</sup>, Warren P. Smith<sup>1</sup> , Shawn B. Honomichl<sup>1</sup> , James F. Bresch<sup>5</sup> , Leslie R. Lait<sup>6</sup> , Yunqian Zhu<sup>7</sup>, Simone Tilmes<sup>1</sup> , Peter R. Colarco<sup>2</sup> , Juying Warner<sup>8</sup> , Adrien Vuvan<sup>9</sup>, Cathy Clerbaux<sup>9</sup> , Elliot L. Atlas<sup>10</sup> , Paul A. Newman<sup>11</sup> , Troy Thornberry<sup>12</sup> , William J. Randel<sup>1</sup> , and Owen B. Toon<sup>7,13</sup> 

### Key Points:

- This model study is conducted in preparation for an airborne field campaign investigating the Asian monsoon transport
- Result shows that eastward eddy shedding of the anticyclone significantly alters upper tropospheric composition over the Western Pacific
- CO seasonal distribution provides a chemical perspective of the monsoon system and sheds new light on monsoon dynamics and circulation

### Supporting Information:

Supporting Information may be found in the online version of this article.

### Correspondence to:

L. L. Pan,  
[liwen@ucar.edu](mailto:liwen@ucar.edu)

### Citation:

Pan, L. L., Kinnison, D., Liang, Q., Chin, M., Santee, M. L., Flemming, J., et al. (2022). A multimodel investigation of Asian summer monsoon UTLS transport over the Western Pacific. *Journal of Geophysical Research: Atmospheres*, 127, e2022JD037511. <https://doi.org/10.1029/2022JD037511>

Received 16 JUL 2022  
Accepted 6 DEC 2022

<sup>1</sup>Atmospheric Chemistry Observations and Modeling Laboratory, National Center for Atmospheric Research, Boulder, CO, USA, <sup>2</sup>Atmospheric Chemistry and Dynamics Laboratory, NASA Goddard Space Flight Center, Greenbelt, MD, USA, <sup>3</sup>Jet Propulsion Laboratory, California Institute of Technology, Pasadena, CA, USA, <sup>4</sup>Copernicus Atmosphere Monitoring Service, European Centre for Medium-Range Weather Forecasts, Reading, UK, <sup>5</sup>Mesoscale and Microscale Meteorology Laboratory, National Center for Atmospheric Research, Boulder, CO, USA, <sup>6</sup>Science Systems and Applications, Inc., Lanham, MD, USA, <sup>7</sup>Laboratory for Atmospheric and Space Physics, University of Colorado at Boulder, Boulder, CO, USA, <sup>8</sup>Department of Atmospheric and Oceanic Science, University of Maryland, College Park, MD, USA, <sup>9</sup>LATMOS/IPSL, Sorbonne Université, UVSQ, CNRS, Paris, France, <sup>10</sup>Rosenstiel School of Marine, Earth, and Atmospheric Science, Department of Atmospheric Sciences, University of Miami, Miami, FL, USA, <sup>11</sup>Earth Sciences Division, NASA Goddard Space Flight Center, Greenbelt, MD, USA, <sup>12</sup>NOAA Chemical Sciences Laboratory, Boulder, CO, USA, <sup>13</sup>Department of Atmospheric and Oceanic Sciences, University of Colorado at Boulder, Boulder, CO, USA

**Abstract** The Asian summer monsoon (ASM) as a chemical transport system is investigated using a suite of models in preparation for an airborne field campaign over the Western Pacific. Results show that the dynamical process of anticyclone eddy shedding in the upper troposphere rapidly transports convectively uplifted Asian boundary layer air masses to the upper troposphere and lower stratosphere over the Western Pacific. The models show that the transported air masses contain significantly enhanced aerosol loading and a complex chemical mixture of trace gases that are relevant to ozone chemistry. The chemical forecast models consistently predict the occurrence of the shedding events, but the predicted concentrations of transported trace gases and aerosols often differ between models. The airborne measurements to be obtained in the field campaign are expected to help reduce the model uncertainties. Furthermore, the large-scale seasonal chemical structure of the monsoon system is obtained from modeled carbon monoxide, a tracer of the convective transport of pollutants, which provides a new perspective of the ASM circulation, complementing the dynamical characterization of the monsoon.

**Plain Language Summary** The Asian summer monsoon has been known as a weather system for centuries, but only in the recent decades has the system been recognized for its importance in atmospheric composition. Monsoon deep convection lofts near surface air to 15–17 km altitudes thus altering the chemical composition of the tropopause layer. The process also sends aerosols and chemically active trace gas species into the stratosphere where they affect climate through their impacts on ozone and aerosol radiative forcing. To understand the monsoon transport process and its impacts on climate system, a large airborne field campaign, the Asian summer monsoon Chemical and Climate Impact Project, was planned. This paper presents a set of results from precampaign model studies. These results serve as the hypotheses for the field investigation and provide guidance for its operational planning.

## 1. Introduction

Fluctuations of the Asian summer monsoon (ASM) impact the lives of billions of people through the variability of precipitation patterns and intensity. Along with this major weather phenomenon is a significant chemical transport pathway that couples surface emissions of the ASM region to global climate and air quality. The coupling of the most polluted boundary layer (BL) on Earth to the largest upper troposphere and lower stratosphere (UTLS) dynamical system in the Northern Hemisphere summer season through deep monsoon convection has the potential to generate significant chemical and climate impacts. The behavior of the ASM as a transport pathway, the chemical composition of the UTLS outflow of the ASM air mass, the amount and properties of UTLS

aerosols associated with the ASM, and the stratospheric water vapor enhancement due to the ASM are among the key elements of the Asian summer monsoon Chemical and Climate Impact Project (ACCLIP). The project is planned to use two high-altitude research aircraft, the National Science Foundation (NSF)/National Center for Atmospheric Research (NCAR) research aircraft Gulfstream V (GV) and the NASA WB-57, to conduct in situ measurements of a wide range of trace gas and aerosol species in the UTLS. Also planned are balloon-borne measurements of aerosol and water vapor profiles to complement the airborne studies. This project follows and complements the Stratospheric and upper tropospheric processes for better Climate predictions (StratoClim; <http://www.stratoclim.org/>) project, which conducted high-altitude research flights from Kathmandu, Nepal, and successfully sampled chemical distributions of a suite of trace gases and aerosols near the center of the ASM anticyclone during July–August 2017 (Adcock et al., 2021; Bucci et al., 2020; Höpfner et al., 2019; Mahnke et al., 2021; von Hobe et al., 2021).

Due to the COVID-19 pandemic, the ACCLIP field campaign was postponed from summer 2020 to 2022. To make productive use of the delay, the ACCLIP science team conducted a multimodel chemical forecasting and flight planning dry run during the 2020 ASM season. The dry run provided the first multimodel investigation of ASM transport from the monsoon anticyclone into the UTLS over the Western Pacific and subsequent transport into the global atmosphere. The resulting information from this study is not only important for ACCLIP project planning, but also sets the stage for discoveries during the campaign and for postcampaign data analysis. The information we are presenting here about this multimodel study should also serve as a useful resource for future campaigns that involve complex chemistry and dynamical meteorology.

Dynamically, the transport process that connects the core region of the ASM anticyclone (centered over the Tibetan Plateau) with the Western Pacific UTLS is associated with eastward eddy shedding of the “parent” (Tibetan) anticyclone and the formation of the Western Pacific Anticyclone (WPA). This anticyclone eddy shedding process in the UT was first identified from low-PV air masses at the 370 K potential temperature level (Popovic & Plumb, 2001). From a different perspective, this process was also identified as a subseasonal east-west oscillation of the ASM anticyclone center between a Tibetan Plateau mode and an Iranian Plateau mode (Y. Liu et al., 2007; Q. Zhang et al., 2002). The implications of these processes for UTLS chemical composition were first identified using satellite water vapor ( $\text{H}_2\text{O}$ ), carbon monoxide (CO), and ozone ( $\text{O}_3$ ) data from the Microwave Limb Sounder (MLS; Garny & Randel, 2013; Yan et al., 2011) and CO in a chemistry climate model (Pan et al., 2016). These earlier works, however, centered on the oscillations between the Tibetan and Iranian modes, or the westward eddy shedding, which was also the focus of Popovic and Plumb (2001). A broader-scale structure of the eddy shedding’s transport impact was later identified using satellite CO data (Luo et al., 2018) and an analysis combining satellite data and trajectory modeling (Honomichl & Pan, 2020). The latter provided the first statistical characterization of the eastward eddy shedding as a significant chemical transport process and identified the WPA as the Western Pacific mode of the ASM anticyclone (Honomichl & Pan, 2020). It is worth noting that a downstream signature of this transport was identified in airborne in situ measurements over the west of Europe in a 2012 field campaign (Müller et al., 2016) with the support of Lagrangian modeling of transport tracers (Vogel et al., 2014). The presence of the WPA, also referred to as the Bonin High, has been studied in the context of the east Asia summer weather pattern (Enomoto, 2004; Enomoto et al., 2003). As pointed out by Enomoto et al. (2003), the Bonin High, referred to as the WPA herein, is associated with negative PV anomalies at the tropopause level and should be distinguished from the North Pacific subtropical anticyclone in the lower troposphere. The latter is often referred to as the Western Pacific subtropical high (e.g., Rodwell & Hoskins, 2001; K. Yang, Cai, et al., 2022). The dynamics of WPA formation and evolution have recently been described by Wang et al. (2022).

The recognition of eastward eddy shedding as a transport process linking the ASM processed air masses to the Western Pacific opened a new opportunity for airborne sampling of the ASM chemical impact in the UTLS. The ACCLIP campaign was planned based on a small set of initial studies and observations (Honomichl & Pan, 2020; Luo et al., 2018; Ungermaun et al., 2016). The 2020 season modeling study results significantly expand and enrich the hypotheses first formulated in the campaign proposal phase. Briefly, we now have substantial evidence that the chemical trace gas and aerosol content of the ASM anticyclone can be sampled from the Western Pacific, owing to the intense transport via subseasonal scale eastward eddy shedding.

**Table 1**  
*Models and Satellite Products Used in the 2022 Forecast Dry Run*

**Meteorological forecast**

NCEP GFS (0.5°)  
NCAR/MMM WRF-ARW (15 km)

**Chemical forecast**

NCAR/ACOM WACCM (1° × 1° × 110 L, interactive chemistry, nudging with GEOS)  
NASA GEOS-FP (0.25° × 0.25° × 70 L)  
ECMWF CAMS (40 km, data assimilation)

**Lagrangian model RDF**

TRAJ3D (GFS winds)

**Satellite products**

HIMAWARI (multichannel)  
MLS (CO, H<sub>2</sub>O, O<sub>3</sub> at 100 and 150 hPa)  
TropOMI (trop CO)  
AIRS (trop CO)  
CrIS (trop CO)  
IASI (trop and UT CO)

In this paper, we present the insights we have obtained through the dry-run and the post-dry-run analysis. The set of questions we aim to address is important not only for the ACCLIP campaign but also for expanding our knowledge of ASM dynamics and transport, as well as its linkage of the Asian BL to the global atmosphere:

- What are the primary convective transport BL origins for shedding air masses over the Western Pacific? What is the transport time scale for these shedding air masses?
- How frequent are eastward shedding events expected to be throughout the planned campaign period?
- How consistent are the models in predicting the spatial and temporal extent of shedding events, and the concentrations of transported chemical and aerosol loadings?
- What is the modeled vertical depth of the ASM transport into the stratosphere throughout the season?

In addition to these questions, we have investigated the contribution from transport by Western Pacific convection, especially tropical cyclones. This process will be the focus of a separate model study.

In addressing these questions here, we aim to provide a comprehensive chemical characterization of the eastward eddy shedding process using models supported by satellite data and meteorological (re)analyses. The results from the set of state-of-the-art models also provide new perspectives on the seasonal-average structure of the ASM transport, chemical perturbations to the global lower stratosphere on seasonal time scales, and the leading ASM convective transport source regions. This new information complements the increasing number of ASM transport modeling studies (e.g., Bossolasco et al., 2021; Gottschaldt et al., 2017; Lee et al., 2021; Pan et al., 2016; Park et al., 2009; Ploeger et al., 2017; Vogel et al., 2014, 2015, 2019; Yu et al., 2017) and provides additional insight into data analysis from recent airborne studies (e.g., Adcock et al., 2021; Bucci et al., 2020; Höpfner et al., 2019; von Hobe et al., 2021) and the analyses of satellite observations in the last decade (e.g., Park et al., 2007, 2008; Randel et al., 2010; Santee et al., 2017).

## 2. Models and Satellite Products Used in the Study

A suite of models and satellite data products are identified for supporting ACCLIP field operations and for postcampaign data analysis and interpretation. These models and products are listed in Table 1. The results of post-dry-run analysis are derived largely from three global chemistry forecast models: NASA Goddard Earth Observing System Forward Processing (GEOS-FP), NCAR Whole Atmosphere Community Climate Model (WACCM), and European Centre for Medium-Range Weather Forecasts (ECMWF) Copernicus Atmosphere Monitoring Service (CAMS). The transport analysis is also heavily supported by the Lagrangian trajectory model

TRAJ3D and the idealized surface tracer in the Weather Research and Forecasting (WRF) model. In addition, the models are supported by the CO data from multiple satellite instruments. A brief description is given in this section for each of the models and products.

## 2.1. Chemical Forecast Models

### 2.1.1. GEOS-FP

The NASA GEOS-FP model (Lucchesi, 2018) is a state-of-the-art numerical weather prediction system that assimilates near-real time observations. The GEOS-FP Atmospheric Data Assimilation System (ADAS) actively assimilates roughly  $2 \times 10^6$  observations for each analysis, including about  $7.5 \times 10^5$  Atmospheric Infrared Sounder (AIRS) radiance data. The GEOS atmospheric general circulation model (AGCM) uses finite-volume dynamics (Lin, 2004) integrated with various physics packages (e.g., Bacmeister et al., 2006), under the Earth System Modeling Framework (ESMF) including the Catchment Land Surface Model (CLSM; e.g., Koster et al., 2000). The assimilation is performed on a cubed-sphere grid at C720 resolution (12 km), and all output products are saved on a “normal” geographic latitude–longitude grid at a horizontal resolution of  $0.3125^\circ$  longitude by  $0.25^\circ$  latitude and at 72 vertical levels, extending to 0.01 hPa. The majority of GEOS-FP data products are time-averaged, but some instantaneous products are also available. Hourly data intervals are used for two-dimensional products, while 3-hourly intervals are used for three-dimensional products. For ACCLIP, 3-hourly instantaneous forecast products for CO and its tagged tracers, SO<sub>2</sub>, and aerosols (including dust, sea salt, sulfate, black carbon [BC], and organic matter) are used for dry-run flight planning and science analysis. The tagged CO tracers, SO<sub>2</sub>, and aerosols in the GEOS model simulations are documented in detail by Bian et al. (2013).

### 2.1.2. WACCM

The Whole Atmosphere Community Climate Model version 6 (WACCM6) is a component of the Community Earth System Model 2 (CESM2) and is described by Gettelman et al. (2019). This “high top” model has 110 levels with a vertical range from the surface to the lower thermosphere (~140 km altitude; Garcia & Richter, 2019). The vertical resolution in the UTLS is 500 m. The horizontal resolution is  $0.95^\circ$  latitude  $\times$   $1.25^\circ$  longitude. For the ACCLIP forecast dry run, the model uses the specified dynamics (SD) option (Lamarque et al., 2012), whereby reanalysis temperature and zonal and meridional winds are used to nudge the model state, thus affecting parameterizations controlling BL exchanges, advective and convective transport, and the hydrological cycle. This model’s dynamical constraints arise from meteorological fields provided by the Modern-Era Retrospective analysis for Research and Applications Version 2 (MERRA-2; Gelaro et al., 2017), and the nudging approach is described by Davis et al. (2022) with a nudging relaxation time constant of 50 hr.

The model represents chemical processes in the troposphere through the lower thermosphere. The chemical species for this run are contained in the O<sub>x</sub>, NO<sub>x</sub>, HO<sub>x</sub>, ClO<sub>x</sub>, and BrO<sub>x</sub> chemical families, along with CH<sub>4</sub> and its degradation products. This mechanism also includes primary nonmethane hydrocarbons and related oxygenated organic compounds. The chemical processes are summarized in detail by Emmons et al. (2020). Reaction rates follow the JPL 2015 recommendations (Burkholder et al., 2015). WACCM6 features prognostic stratospheric aerosols (Mills et al., 2017) using a modal aerosol model (MAM, X. Liu et al., 2016), which has been modified to change the mode widths and allow growth of sulfate aerosol into the coarse, or large size, mode (MAM4). This is important to properly represent aerosol sources in the stratosphere, including volcanic emissions, and natural background emissions of carbonyl sulfide (OCS), which form the stratospheric aerosol layer. The current mechanism includes a new detailed representation of secondary organic aerosols (SOAs), based on the “simple VBS” approach (Tilmes et al., 2019). The photolytic reactions are based on both inline chemical modules and a lookup table approach (Kinnison et al., 2007). The WACCM mechanism includes a total of 231 species and 583 chemical reactions broken down into 150 photolysis reactions, 403 gas-phase reactions, 13 tropospheric, and 17 stratospheric heterogeneous reactions. Anthropogenic surface emissions are from the global CAMS (see below) emission data set version 4. Fire emissions are based on the FINN inventory Version 1.5 (Wiedinmyer et al., 2011). The volcanic SO<sub>2</sub> emissions are derived for each volcanic eruption using the Neely and Schmidt (2016) database updated through the year 2020.

### 2.1.3. CAMS

The CAMS (<https://atmosphere.copernicus.eu/>) provides twice daily global forecast and analysis of atmospheric composition using the Integrated Forecasting System (IFS) of the ECMWF. For the operational CAMS forecast, the IFS simulates the sink and source processes of tropospheric trace gases (Flemming et al., 2015) and aerosols (Rémy et al., 2019) in addition to the weather forecast parameters. The IFS uses a semi-Lagrangian advection scheme and a convective-mass flux scheme (Bechtold et al., 2014) for the simulation of the transport of all tracers. The monthly mean CAMS-GLOB data (Granier et al., 2019) were used for the anthropogenic, biogenic, and soil emissions. The Global Fire and Assimilation System (GFAS; Kaiser et al., 2012) provides daily wildfire emissions based on MODIS fire radiative power observations (Kaiser et al., 2012). The IFS in the CAMS configuration assimilates a wide range of satellite observations of CO, O<sub>3</sub>, nitrogen dioxide (NO<sub>2</sub>), and aerosol optical depths using the incremental 4D-Var approach of the IFS (Benedetti et al., 2009; Inness et al., 2015). The assimilated and passively monitored satellite measurements of atmospheric composition can be found at the CAMS satellite monitoring web pages ([https://atmosphere.copernicus.eu/charts/cams\\_monitoring](https://atmosphere.copernicus.eu/charts/cams_monitoring)). Specifically in 2021, retrievals from MOPITT and Infrared Atmospheric Sounding Interferometer (IASI) were assimilated to improve the CO initial conditions of the CAMS forecasts. For the meteorological initial conditions (analysis), the same in situ, remote sensing, and satellite observations are assimilated as in ECMWF's operational high-resolution weather forecasts (HRES). The main differences between HRES and the global CAMS forecast with the IFS is the coarser horizontal resolution of the CAMS forecast (40 km vs. 9 km), while the number of vertical levels (137 with the model top ~80 km) is the same. Further differences are (a) the use of a simplified representation of the numerical weather prediction background errors and (b) the use of prognostic aerosol and ozone in the IFS radiation scheme in the CAMS forecasts. HRES use dynamically varying background errors for the weather parameters and aerosol and ozone climatologies in the radiation scheme.

## 2.2. Other Models

### 2.2.1. WRF-ARW and Idealized Surface Tracers

To forecast the mesoscale meteorological circulation and the regional transport of BL air, the Advanced Research version of the Weather Research and Forecasting model (WRF-ARW; Skamarock et al., 2019) version 4.1.1 was included in the suite of forecast models. The model grid, covering the entire region of east Asia and the Western Pacific, consists of 662 × 386 horizontal grid points with a spacing of 15 km and 52 vertical levels between the surface and 20 hPa. The runs were initialized at 0000 and 1200 UTC each day using NCEP Global Forecast System (GFS; NOAA, 2021) 0.25° output interpolated to the WRF grid. Forecasts were run for 144 hr with lateral boundary conditions supplied by the GFS. The model uses the Kain-Fritsch convective parameterization, the WRF double-moment microphysics scheme (WDM6), the Yonsei University (YSU; Hong et al., 2006) planetary BL scheme, and the Rapid Radiative Transfer radiation scheme (RRTMG).

Convective transport information was provided by a set of idealized BL tracers as described by Barth et al. (2012). These tracers were continuously released in four designated regions: East China, Southeast Asia, Plateau South Flank, and West Pacific, as shown in Figure S1 in Supporting Information S1. The tracer had a constant value of unity throughout the model-predicted BL and was transported by WRF's physical and dynamical processes without impacting the model simulation. Tracer concentrations in the UT from each designated region of release provide diagnostics for the contributing BL top and the process of convective uplifting.

### 2.2.2. TRAJ3D

To complement the forward model forecast of transport from the regional BL, a back trajectory based reverse domain filling (RDF; e.g., Schoeberl & Newman, 1995) approach is used to forecast the regional BL origins of the UTLS air mass over the campaign domain. This RDF forecast was produced using the TRAJ3D model, which is a computationally efficient three-dimensional trajectory model developed at Texas A&M (Bowman, 1993; Bowman & Carrie, 2002). During the dry run, RDF was designed to forecast the regional BL contribution from the four designated regions (as shown in Figure S1 in Supporting Information S1) within 15 days of transit time. This was implemented by calculating the kinematic back trajectories of air parcels initialized in the UTLS over the campaign domain using TRAJ3D driven by the forecasted 3D wind fields from NCEP GFS operational analysis (NOAA, 2021). The back trajectories are initiated at 0.5° spatial intervals in both latitude and longitude at the 100, 150, and 200 hPa pressure levels every 6 hr. The RDF forecast therefore provides information on rapid (i.e.,

convective) transport from the monsoon regional BL based on resolved wind fields. An example of the RDF forecast at 150 hPa is shown in Figure S1 in Supporting Information S1. In post-dry-run analysis, the back trajectories are calculated using TRAJ3D driven by ERA5 (Hersbach et al., 2020) reanalysis wind fields. Resulting diagnosis of transit times and contributing BL regions is presented in Section 3.

### 2.3. Meteorological Forecast Products

Standard meteorological forecast products were produced from the NCEP GFS (NOAA, 2021) and from the NCAR WRF-ARW (described in Section 2.2). Products such as geopotential height (GPH) and winds at various pressure levels, sea-level pressure and rainfall, and cloud forecasts were created to depict the weather systems over the study region.

### 2.4. Satellite Information as References for Model Representation

To support the chemical forecast, multiple satellite data sets contributed to the dry run as listed in Table 1.

#### 2.4.1. MLS

The primary data set contributing to the post-dry-run analysis reported in this paper is CO from the Aura Microwave Limb Sounder. MLS measurements have been used in a number of prior ASM studies (see Santee et al., 2017, and references therein). Here, we use version 4.2 (v4.2) MLS measurements (Livesey et al., 2020). Although an updated MLS data set (v5) was released in June 2020, it was not used for the dry run that summer because reprocessing with the v5 retrieval algorithms of the entire MLS data record (needed to calculate the climatological fields against which the 2020 season's variations were compared) had not been completed at that time. MLS v4 and v5 CO products generally agree closely in the UTLS. MLS v4 H<sub>2</sub>O and O<sub>3</sub> measurements were also analyzed as part of the dry run.

#### 2.4.2. IASI

Satellite CO data from the IASI (Clerbaux et al., 2009) are also used to identify shedding events over the Western Pacific. The IASI CO vertical profiles have been validated against aircraft and other satellite data (George et al., 2015), and it was shown that most of its sensitivity is coming from the mid troposphere. But as demonstrated by Luo et al. (2018), this nadir-sounding instrument is able to resolve the CO enhancement in a UT layer even though it has a relatively weak CO retrieval information in the UT. The much higher density of the IASI horizontal sampling (more than 1.2 million observations per day) complements the limb sounder.

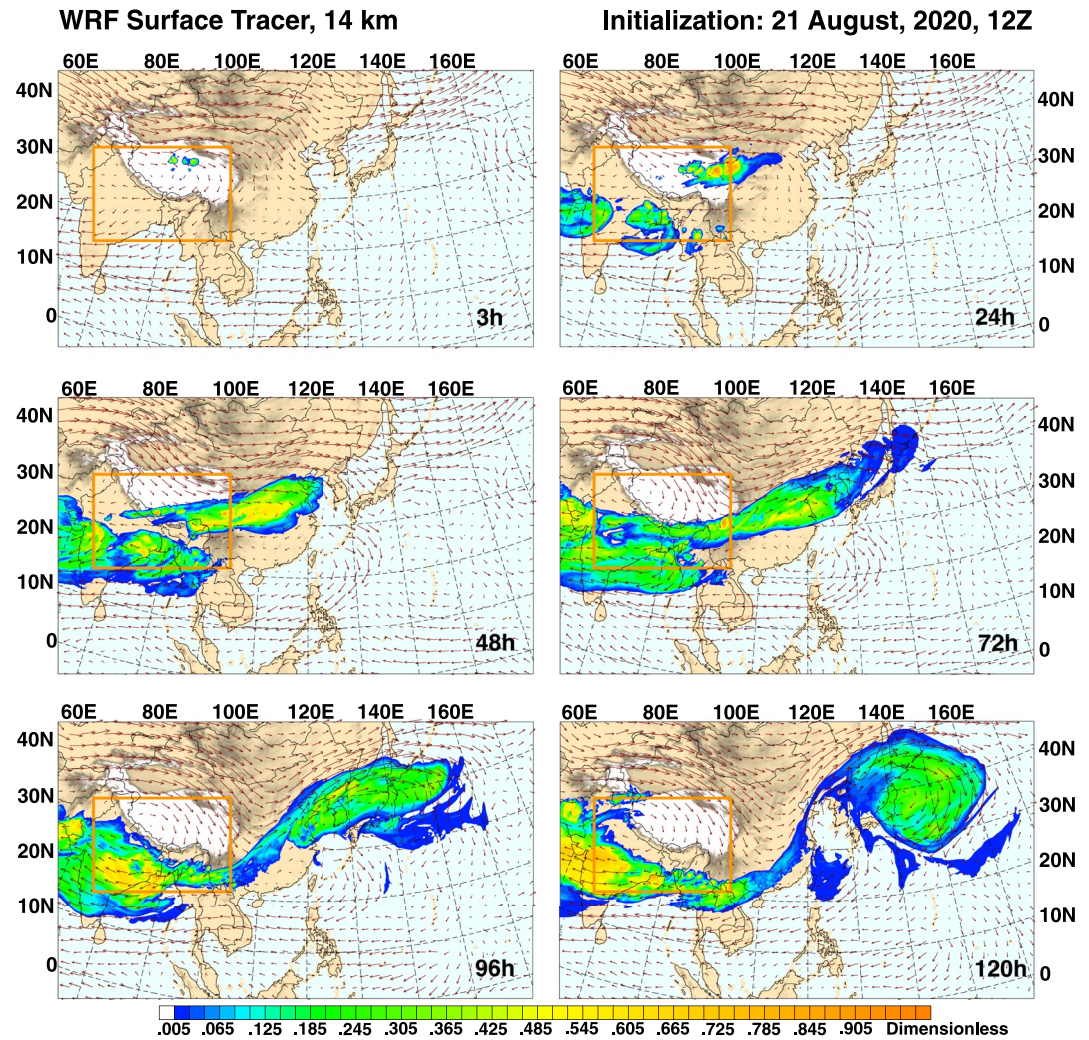
#### 2.4.3. AIRS, CrIS, and TROPOMI

To provide references for tropospheric CO in Asia and to monitor possible strong emission events, three satellite data sets for tropospheric CO columns were also included in the dry-run exercise. These are the AIRS (Aumann et al., 2003), the Cross-track Infrared Sounder (CrIS; Goldberg et al., 2013), and TROPospheric Monitoring Instrument (TROPOMI; Borsdorff et al., 2019). AIRS and CrIS are primarily sensitive to midtropospheric CO and provide similar CO column products. TROPOMI, on the other hand, provides a mix of near-surface and free-tropospheric concentrations.

## 3. Eastward Eddy Shedding

Transport associated with eastward eddy shedding is a significant component of the overall ASM dynamics and its impact on UTLS composition. In this section, we begin by diagnosing the air mass connection between the Asian BL and the Western Pacific UTLS. Two complementary diagnostics are presented. One follows the air masses from the Asian BL in an eastward shedding event (forward), and the other traces the air masses over the Western Pacific UTLS backward to identify the primary region from which they left the BL. Evolution of a shedding event at the tropopause level is then shown by an example using complementary observations, followed by an example chemistry model representation of the shedding event. Finally, we characterize the occurrence of shedding events for the 2020 ASM season using modeled UT CO.

Dynamically, eddy shedding in the UT has been described as instability of the parent anticyclone associated with the convectively forced low-PV air (Garny & Randel, 2013; Popovic & Plumb, 2001). As a transport process, this

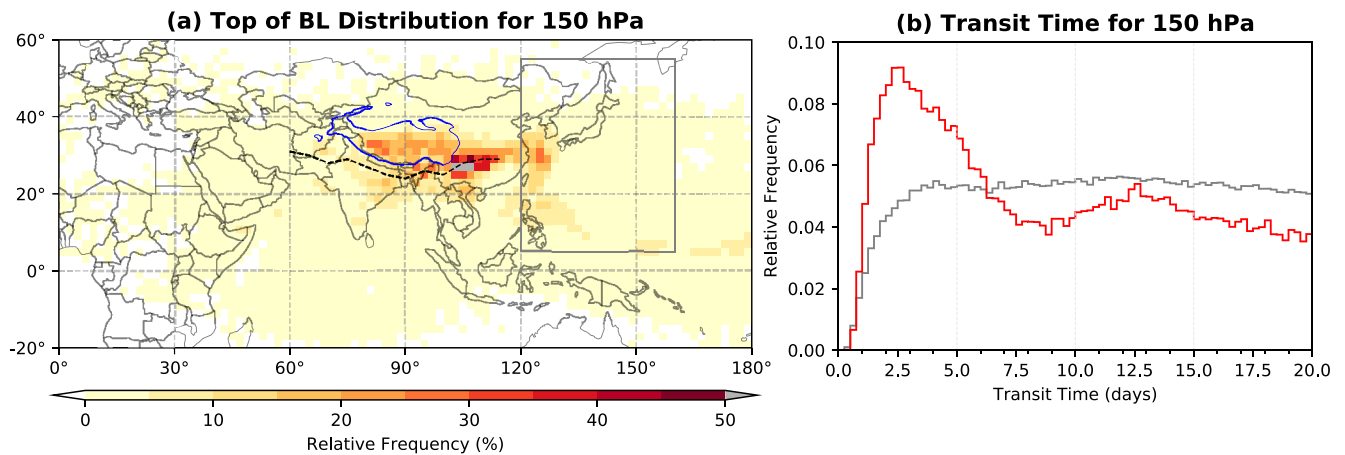


**Figure 1.** Weather Research and Forecasting (WRF) model forecast of an idealized surface tracer, initiated from the region marked by the orange box (designated as “Plateau South Flank,” see Figure S1 in Supporting Information S1), at 14 km at six forecast time steps. The results illustrate the significant contribution of the region’s boundary layer to the northwestern Pacific UT through an eastward shedding event.

scenario can be described as convection lofting BL air to the UT, followed by the shedding event transporting these lofted air masses east-west quasi-isentropically at the top of convection. Here, we elucidate this process using an idealized surface tracer modeled in WRF-ARW (described in Section 2). Figure 1 shows the distribution of this idealized surface tracer, initiated in the BL within a region defined as “Plateau South Flank,” at 14 km altitude for six time steps from 3 to 120 hr. At the 120-hr (5-day) step, a large “blob” of the tracer is over the northwestern Pacific, east of Japan. The wind field overlaid with the tracer indicates the collocation of the tracer with the WPA. The transport transit time in this example, ~5 days, is representative of other events.

The identification of this Plateau South Flank BL region as the primary source contribution to the anticyclone-confined air mass is consistent with past studies. In a back trajectory analysis, Bergman et al. (2013) identified a “conduit,” centered in the region at the southeastern edge of the Tibetan Plateau, for air masses entering the ASM anticyclone. In a Lagrangian model study using a boundary emission tracer, Vogel et al. (2015) identified the region of Northern India and Southern China as the leading source. From an entirely different approach, this region was shown to be the center of the “chimney” in the convective transport of CO using a chemistry model (Pan et al., 2016). Trajectory statistics have also shown that this is within the transport “hot spot” (southeastern side of the Plateau and north side of the Bay of Bengal) for the air masses in the WPA to pass through the





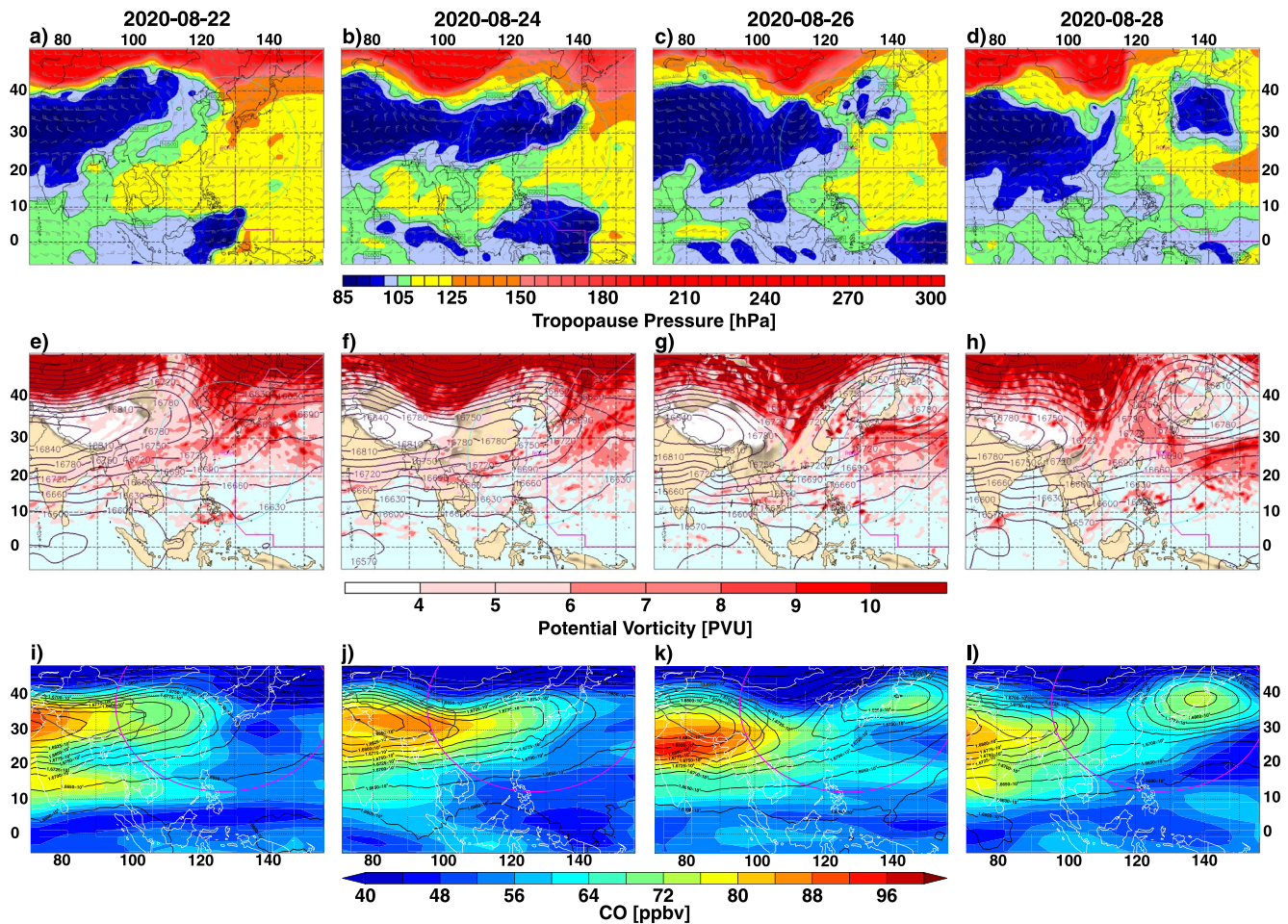
**Figure 2.** Trajectory model diagnosis of the boundary layer (BL) origin (a) and transit times (b) for the UT air mass over the northwestern Pacific domain (indicated by the gray rectangle). The relative frequency distribution map (a) shows the BL contribution to the 150 hPa level air mass in the domain within 20 days of transit time based on the back trajectory analysis. The Tibetan Plateau is marked by the thin blue line, and the monsoon trough of the season, analyzed using surface pressure data of July–August 2020, is shown by the black dashed line. The two transit-time distributions (TTDs) within the 20 days (b) represent the air parcels for the entire domain (gray) and those filtered using a geopotential height (GPH) threshold value (red; see text), respectively. The relative frequency for each distribution is normalized within the 20 days. The TTDs are given in 6-hr bins.

regional BL (Honomichl & Pan, 2020). The example in Figure 1 demonstrates the process of convective lofting in this BL region and subsequent eastward transport into the Western Pacific UT.

Among the four designated regions, the idealized surface tracer released from the East China box (see Figure S1 in Supporting Information S1) also makes a significant contribution to the Western Pacific UT, often mixed with the Plateau South Flank tracer. The Southeast Asia tracer, on the other hand, has relatively little contribution over the Western Pacific, largely because Southeast Asia's upper-level flow is dominated by the easterly jet. The tracer from the Western Pacific region shows a significant contribution associated with tropical cyclone activity.

Although back trajectory statistics of BL transport origin for the UT WPA have been reported in a previous study (Honomichl & Pan, 2020), here we present a refined analysis for a broader Western Pacific domain (the domain for ACCLIP) for the 2020 July–August season. In this analysis, the back trajectories are calculated for air parcels initialized over the domain ( $120^{\circ}$ – $160^{\circ}$ E;  $5^{\circ}$ – $55^{\circ}$ N; gray rectangle in Figure 2) at  $0.5^{\circ}$  spacing, multiple pressure levels, and in 6-hr intervals from 1 July to 31 August 2020. The calculation is done using the trajectory model TRAJ3D (described in Section 2) driven by 3D kinematic winds from ERA5 reanalysis with  $0.25^{\circ}$  resolution and 1 hourly time interval. Although we have examined the results from 60-day back trajectories at multiple pressure levels, in Figure 2 we show the BL source distribution map and transit-time distributions (TTDs, a.k.a. “age spectra”) within the first 20-day (to focus on “rapid transport”) for air parcels initialized at the 150 hPa level. The BL source regions are identified in the relative frequency distribution map, which shows where the back trajectories initialized within the study domain intercepted the top of the BL (defined as the level of 87% of the surface pressure, following Bergman et al. [2013] and Honomichl and Pan [2020]). The TTDs are calculated using trajectory length for the parcels reaching the BL top within 20 days. The gray line indicates the TTD from all air parcels within the domain (gray rectangle), while the red line shows the TTD for air parcels filtered using a GPH threshold to select only those air parcels with 150 hPa GPH higher than 14.35 km. This filter is used as a proxy for identifying the air masses either within the anticyclone or in the eddy shedding. The TTD for the filtered air parcels corresponds roughly to the analysis of Honomichl and Pan (2020, their Figure 9), where the result has shown a similar distribution for the contributing BL, highlighting contributions from both ASM convection and Western Pacific tropical cyclones. The entrainment of air lofted by the Western Pacific tropical cyclone into the ASM anticyclone has been previously identified by trajectory model studies (e.g., Bergman et al., 2013). Observationally, this process has been identified by an ozonesonde analysis with trajectory modeling support (D. Li et al., 2021).

There are two significant refinements in this approach over the previous study (Honomichl & Pan, 2020). First, the high spatial and temporal resolution of the ERA5 reanalysis winds improve the trajectory model representation of convective transport over the ERA-interim data ( $0.7^{\circ}$  and 6 hourly, Dee et al., 2011) used in the earlier



**Figure 3.** Dynamical structure of the tropopause region during a shedding event (22–28 August 2020) from tropopause pressure, 100 hPa PV distribution, and daily 100 hPa CO distribution interpolated from Microwave Limb Sounder (MLS) data. (top row) World Meteorological Organization (WMO) lapse rate tropopause pressure from the Global Forecast System (GFS) analysis. Dark blue highlights the region of the tropopause higher than (i.e., at pressures lower than) 100 hPa. (center row) 100 hPa geopotential height (GPH; overlaid black contours) and PV fields (color fill) from the GFS analysis. (bottom row) Interpolated daily MLS CO data at 100 hPa with the GPH from GFS. The relatively sparse daily along-track data have been mapped onto a regular grid. The magenta ring shows the nominal range of the research aircraft with Osan, ROK as the base of Asian summer monsoon Chemical and Climate Impact Project (ACCLIP) operations.

study, as demonstrated by Smith et al. (2021). This improved representation is likely a key factor revealing the association of the primary region from which the air mass left the BL with the monsoon trough, the region known for deep convection and heavy rainfall (e.g., Krishnamurti & Bhalmé, 1976). This identification shows the physical consistency for the dominant location of convective transport, a connection was not made in previous studies (Bergman et al., 2013; Honomichl & Pan, 2020; Pan et al., 2016).

Second, the use of a broader domain provides a good contrast between background and shedding air masses in terms of their transport times, as shown by the filtered (red) versus background (gray) TTDs. The two distributions have very different transport time scales. The trajectory calculations indicate that 57% of all air parcels leaving the top of the BL, primarily over Asia, reach the 150 hPa level over the Western Pacific within 20 days; for 60 days, the number is 91%. The corresponding percentages for the unfiltered air parcels are approximately 30% for 20 days and 67% for 60 days. The mode in the filtered TTD is around 2 days and the distribution has a width of approximately a week. Note that the GPH filtering only approximately identifies the “younger” shedding air masses because of the small-scale mixing during the shedding process, which is hinted at in Figure 3, where the high-PV stratospheric (older) air mixes into the high-GPH (shedding) region. The TTD (age spectrum) represented by the red curve therefore also includes an unquantified portion of older air masses.

Having established the connection between eastward shedding and the Asian BL, especially the connection with the region along the monsoon trough, we show in Figure 3 the evolution of a shedding event at the tropopause level for a period of a week in late August 2020. The dynamical structure of anticyclonic shedding shows a bulging tropopause (described as a “doming tropopause” in Popovic and Plumb [2001]). We characterize this structure by the tropopause pressure and PV distribution at 100 hPa, both from GFS operational analysis. The effect of the structure on chemical composition is shown using CO from MLS.

Together, these three fields form a consistent picture on a broad scale: during an eastward shedding event, the bulging tropopause structure associated with the ASM anticyclone migrates eastward into the region over the northwestern Pacific and breaks off toward the end of the event. The Rossby wave activity that created this structure is shown by the 100 hPa PV distribution, which marks the propagation of the anticyclonic circulation from the Tibetan mode to the Western Pacific mode and the subsequent formation of the Bonin High (Wang et al., 2022). The PV field also identifies the region dominated by low-PV tropospheric air at the 100 hPa level within the anticyclone and high-PV stratospheric air wrapping around the eastern edge of the anticyclone, intruding into subtropical latitudes (Randel & Park, 2006). The distribution of enhanced CO at 100 hPa shows the constituent transport associated with the shedding and the separation of the shed air mass from the main ASM anticyclone.

Using this late August 2020 period, we examine the representation of the shedding process in the three global chemical forecast models identified for the ACCLIP campaign operations. In Figure 4, we show 150 hPa CO from the three models, GEOS-FP, WACCM, and CAMS, for 26 August 2020 (within the period shown in Figure 3), together with two maps of the CO distributions based on the MLS 147 hPa product and the IASI 12–15 km layer product.

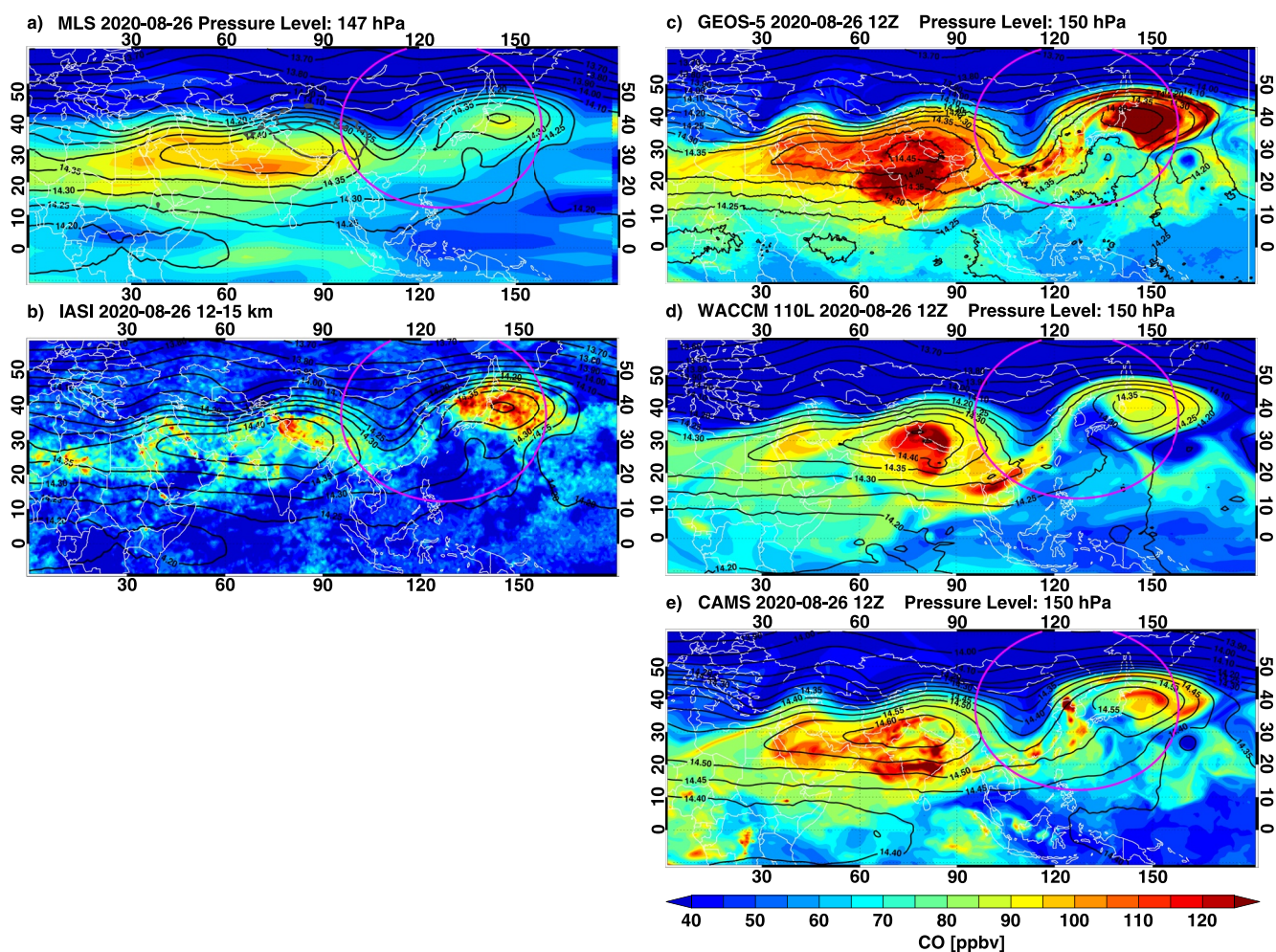
The quantitative differences between the CO maps produced from MLS and IASI data are expected, since the two instruments use very different observing geometries—respectively limb and nadir sounding (Luo et al., 2018). The important message here is that the locations and morphologies of the shedding air masses as represented by the observed UT CO products are reasonably consistent. Similarly, we see general consistency in the three model representations of the shedding location, which engenders confidence in our ability to identify the targeted processes. The quantitative differences provide a desirable spectrum of reference for the airborne sampling. The use of multiple models provides operational robustness in forecasting capability. Note that detailed model inter-comparison is not an objective of this work.

The snapshots and event evolution we have shown identify the location of the target air masses for the ACCLIP project. We examine next the time scales for the occurrence of shedding events throughout an ASM season. Figure 5 is a “time–longitude” Hovmöller diagram for 7 weeks from mid-July to the end of August 2020, the period of the ASM season targeted by the ACCLIP campaign. This diagram is constructed using 150 hPa GPH and CO from GEOS-FP. Shedding events, both eastward and westward, are identified by positive anomalies of CO, which are correlated with positive GPH anomalies. Note that the longitudinal segment of the Tibetan Plateau (approximately 80°–100°E), which is the primary location of convective uplifting and the source region for constituents identified in the shedding air masses (Luo et al., 2018; Pan et al., 2016), is marked by persistent positive CO anomalies throughout the season.

Figure 5 indicates that the frequency of eastward shedding events is quasi-weekly for this season (~6 events in 45 days). The chemical signature of the events persists for 3–9 days in the campaign domain. There should be, therefore, sufficient opportunities for the campaign to sample shedding air masses. The figure further highlights that eastward shedding intensifies toward the second half of August, at least in 2020.

#### 4. Chemical Trace Gas and Aerosol Content Within the Eddy Shedding Air Mass

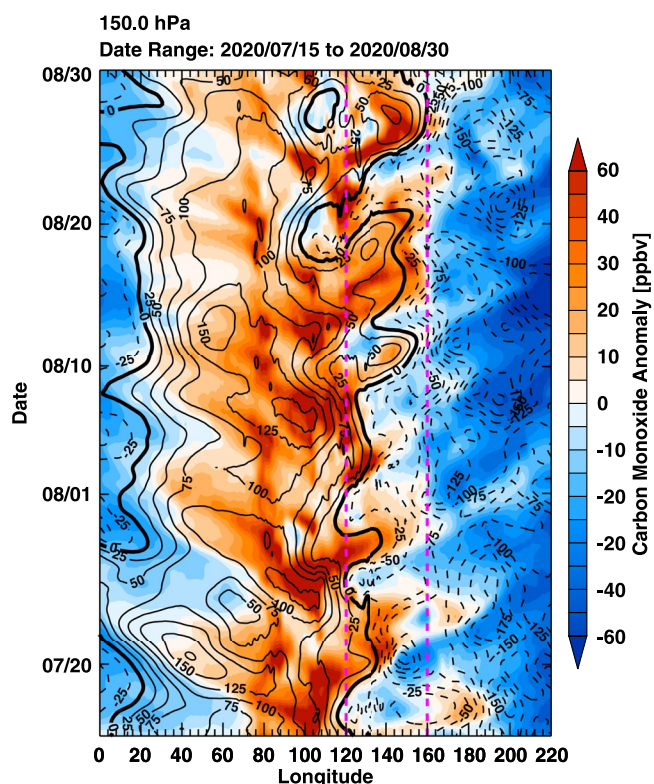
Up to this point, we have used CO to represent the chemical signature of the eddy shedding. CO is an effective tracer of convective transport of pollutants, because it has strong emission sources in both human activities and biomass burning and its lifetime is relatively short. Although the global-average lifetime of CO is estimated to be 2 months (e.g., Duncan et al., 2007; Khalil & Rasmussen, 1990), within the ASM anticyclone its UT lifetime can be much shorter. A snapshot from a WACCM model calculation shows the lifetime of CO in the core region of the anticyclone to be ~1 month (Figure S2 in Supporting Information S1). CO is closely tied to the photochemistry of ozone and aerosols. These factors, combined with the widely available satellite CO data, make CO the most



**Figure 4.** A snapshot of an eddy shedding event (26 August 2020) shown by Microwave Limb Sounder (MLS) and Infrared Atmospheric Sounding Interferometer (IASI) satellite data (left) and the Goddard Earth Observing System Forward Processing (GEOS-FP), Whole Atmosphere Community Climate Model (WACCM), and Copernicus Atmosphere Monitoring Service (CAMS) models (right). The eastward shedding air mass is highlighted by the enhanced CO from satellite observations in both MLS (limb viewing) and IASI (nadir) data. Also included are selected 150 hPa geopotential height (GPH) contours (black). GPH from Global Forecast System (GFS) is used for the MLS and IASI maps.

used chemical tracer in ASM transport studies (e.g., Bucci et al., 2020; Q. Li et al., 2005; Pan et al., 2016; Park et al., 2007, 2009; von Hobe et al., 2021; Y. Yang, Li, et al., 2022). An important goal of the airborne campaign is to investigate the chemical complexity of ASM-related transport, using CO as a primary tracer for the air mass, to quantitatively characterize the ASM-driven UTLS chemical distributions in both gas phase and aerosols. The species of particular interest are those contributing to ozone chemistry in the UT, the very short-lived substances (VSLs) relevant for stratospheric ozone, the species contributing to aerosol formation, and the species necessary for diagnosing the role of the ASM in atmospheric oxidation capacity. This last point was the focus of a model study combining airborne in situ measurements from the Oxidation Mechanisms Observation campaign (Lelieveld et al., 2018).

To set the stage for this investigation, we have inspected a large suite of chemical species in gas phase and aerosols available in the models involved in this study. Figure 6 shows a snapshot of nine selected species at 150 hPa for 27 August 2020 from WACCM. The distributions of these species all have a clear signature of shedding. Together, they highlight the chemical complexity of the UT air mass driven by the ASM transport. While the depressed ozone abundances in the shedding air mass suggest that ASM transport contributes to lowering UT ozone, the elevated levels of key ozone precursors in the shedding air mass, including  $\text{NO}_x$ , CO,  $\text{C}_2\text{H}_6$ , and  $\text{C}_3\text{H}_8$ , suggest that the ASM air mass will contribute to increased UT ozone production. Chemically, the large enhancement of  $\text{CH}_2\text{O}$ , a very short-lived (lifetime  $\sim 0.5$  days) key intermediate volatile organic compound (VOC) degradation



**Figure 5.** Seasonal evolution of the Asian summer monsoon (ASM) anticyclone eastward and westward eddy shedding captured by the CO (color scale) and geopotential height (GPH; black line) anomalies from the Goddard Earth Observing System Forward Processing (GEOS-FP) model at 150 hPa, using once-daily model output. The anomalies are calculated against the respective mean values of GPH or CO along the ridge over the longitude range of 0°–220°E. The longitudinal range of the Asian summer monsoon Chemical and Climate Impact Project (ACCLIP) campaign domain is marked by the two parallel dashed lines (magenta).

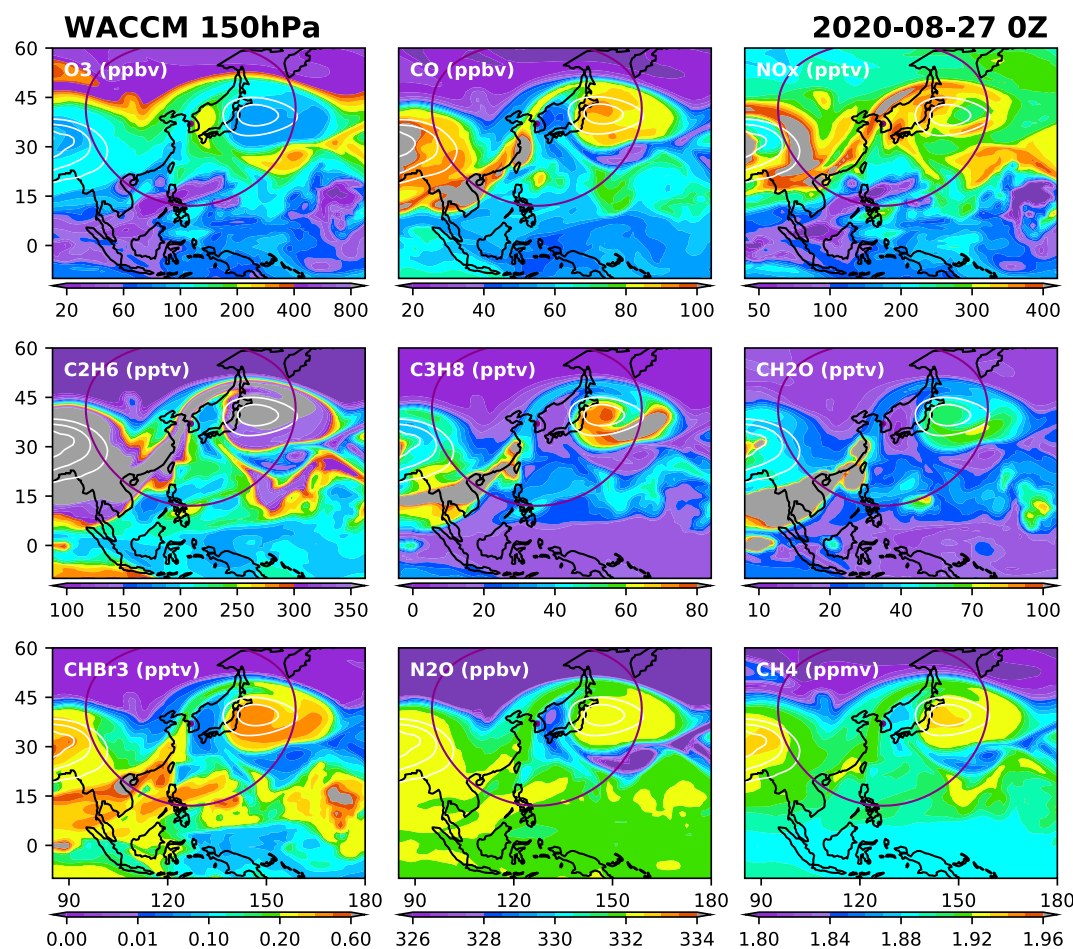
product, within the shedding air mass suggests active VOC oxidation. From a transport point of view, the large enhancement of  $\text{CHBr}_3$ , a VLSL source gas, indicates that marine air is also mixed in with continental pollution, lofted to the UTLS, and redistributed by the monsoon circulation. Enhancement of both short-lived species and very long-lived greenhouse gases  $\text{N}_2\text{O}$  and  $\text{CH}_4$ , compared to the background UTLS, indicates that efficient ASM vertical transport connects the BL to the UT.

The chemical complexity of the shedding air mass in terms of differences in lifetimes, emission origins, and their roles in ozone photochemistry underscores the importance of chemical modeling. Integrating airborne in situ observations and modeling is essential for in-depth understanding of the chemical evolution within these shedding events and therefore the chemical impact of the ASM transport.

In addition to the enhanced BL trace gas species, the role of the ASM in creating a unique and recurring aerosol layer around the tropopause level is an important scientific issue motivating the ACCLIP campaign. This aerosol layer, referred to as the Asian Tropopause Aerosol Layer (ATAL), was initially discovered by satellite data analysis (Vernier, Thomason, & Kar, 2011; Vernier, Thomason, Pommereau, et al., 2011; Thomason & Vernier, 2013) and has been investigated since using satellite, balloon-borne, and ground-based measurements as well as modeling (e.g., Brunamonti et al., 2018; Vernier et al., 2015, 2018; Yu et al., 2017; J. Zhang et al., 2020). The most notable information gap is the chemical composition and particle size distribution of the aerosols, which are critical for diagnosing ATAL formation and maintenance mechanisms and their radiative effects. Information on these parameters is critically needed for improving model representation. The StratoClim campaign obtained the first significant set of airborne in situ and remote-sensing aerosol data in the ATAL (Höpfner et al., 2019; Mahnke et al., 2021; Weigel, Mahnke, Baumgartner, Dragoneas, et al., 2021; Weigel, Mahnke, Baumgartner, Krämer, et al., 2021) from Kathmandu-based research flights. These measurements sampled the South Asian region including Nepal, Pakistan, northern India, and the Bay of Bengal. The data identified a unique characteristic of aerosol composition as containing a significant amount of ammonium nitrate ( $\text{NH}_4\text{NO}_3$ ), and it was found to be associated with a high concentration of gas-phase ammonia ( $\text{NH}_3$ ) in the UT (Höpfner et al., 2019).

The StratoClim flight domain is in the vicinity of the major source region for the air mass confined in the anticyclone (e.g., Bergman et al., 2013; Honomichl & Pan, 2020; Pan et al., 2016; Vogel et al., 2015). The air mass sampled in this region is expected to have strong influence from recent convection and typically consists of younger air (Bucci et al., 2020; Lee et al., 2021; Legras & Bucci, 2020). The tracers from the WRF model and trajectory statistics in Figures 1 and 2 suggest that the air masses associated with eastward shedding events over the Western Pacific share similar BL origins with those sampled by the StratoClim flights. Characterizing the vertical structure, particle size distribution, and chemical composition of the aerosol layer over the Western Pacific will expand the overall understanding of ATAL formation and maintenance.

Figure 7 shows selected aerosol variables from WACCM and GEOS-FP for the same day (27 August 2020) as Figure 6 but for the 100 hPa level. All fields show qualitative consistency in elevated aerosol loading in the shedding air mass, which supports the hypothesis that the ASM aerosol content can be sampled from the Western Pacific. The large quantitative difference in BC mass concentrations from the two models provides a perspective of large model uncertainty. Since BC measurements in the UT are very limited, we expect the ACCLIP campaign to provide much-needed observational constraints for improving model representation of ATAL aerosol. Model results suggest that the aerosols in the shedding air mass will show increased primary and secondary aerosols,



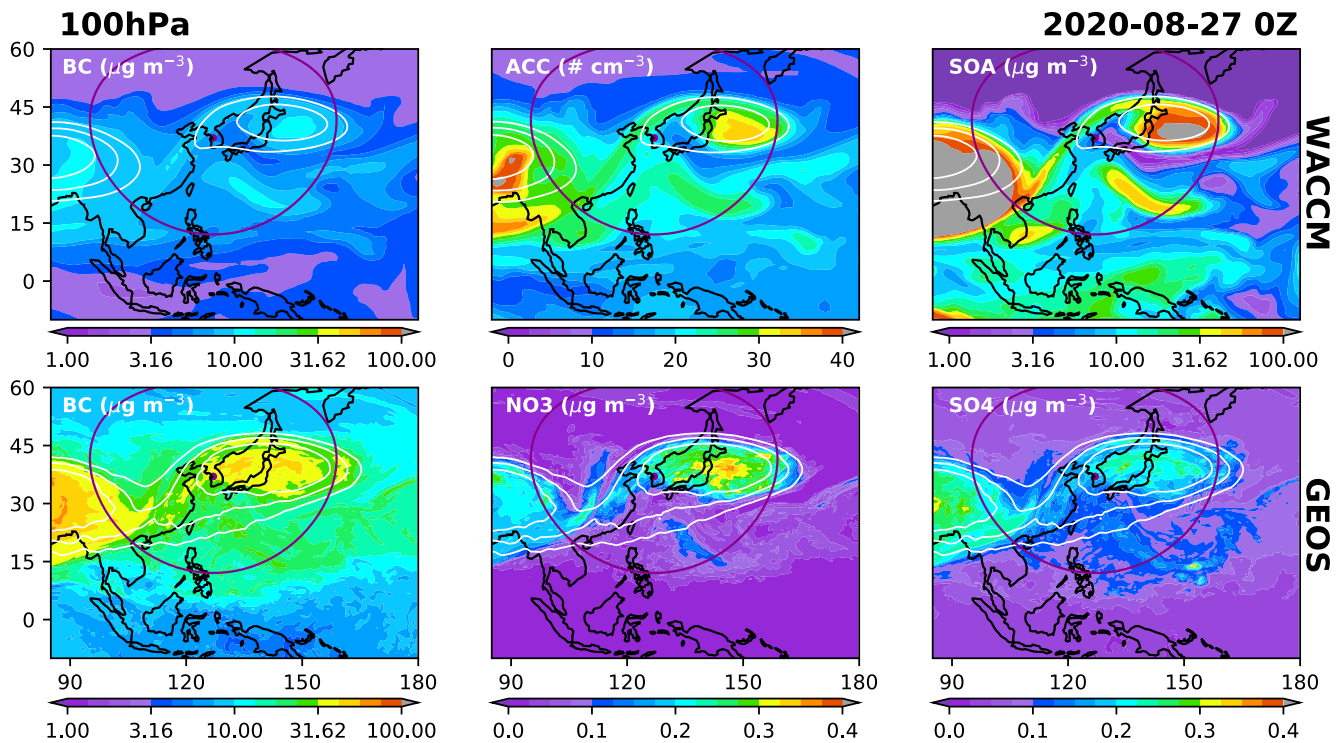
**Figure 6.** Chemical trace gas content in the shedding air mass from the Whole Atmosphere Community Climate Model (WACCM) at 150 hPa. Example of 27 August 2020. The nine selected species from WACCM highlight the impact of the shedding event on the composition of the UT near the tropopause. Selected geopotential height (GPH) contours (14,300, 14,340, and 14,380 m), at 150 hPa are overlaid to indicate the anticyclone shedding.

as well as elevated organic carbon and sulfate concentrations that are clearly distinguished from background aerosols in the UT and the LS.

### 5. Vertical Structure and the Depth of the ASM Transport Into Stratosphere

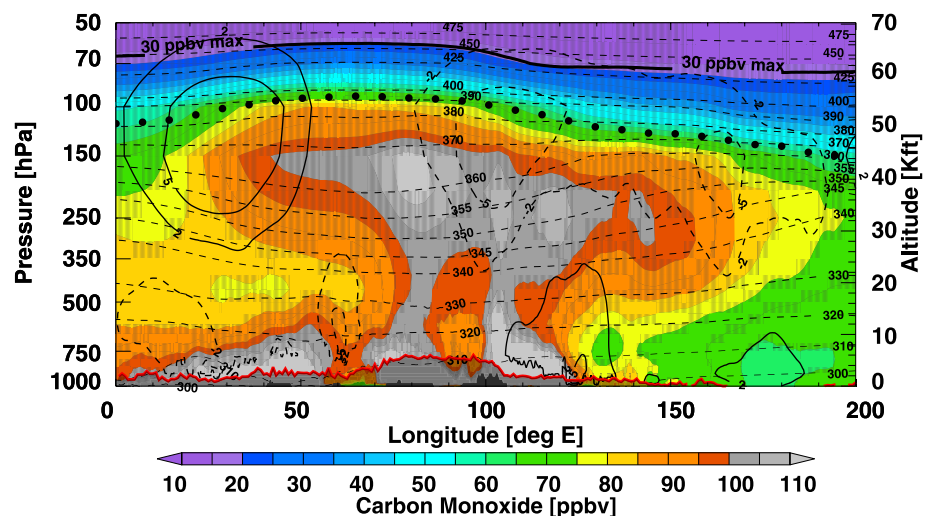
So far, we have primarily focused on the eastward eddy shedding chemical signature at the 150 hPa level, which is approximately 14.5 km and 360–370 K potential temperature. This level represents the top of significant convective transport in the core region of the anticyclone as shown in recent in situ observations (e.g., Mahnke et al., 2021; von Hobe et al., 2021). From the perspective of the ASM dynamical structure, this is also the center level of anticyclone confinement (e.g., Pan et al., 2016; Randel & Park, 2006).

In Figure 8, we present the chemical structure of the ASM system using CO from GEOS-FP averaged for the period of mid-July to the end of August. The distribution of average CO in this cross section appears to have a “mushroom” shape. The core of the “mushroom” appears to have two “stems,” one centered on 80°E, the other 105°E, which correspond well with the longitudes of the persistent positive CO anomalies at 150 hPa throughout the season shown in Figure 5. This “two-stem” structure is also shown in previous work using MERRA reanalysis data (Lau et al., 2018), where the two “stems” are associated with the persistent convective transport over northern India and the southern edge of the Tibetan Plateau, and over southwestern China including the Sichuan Basin, respectively. These locations along the monsoon trough (Figure 2) are known as “hot spots” of deep convective

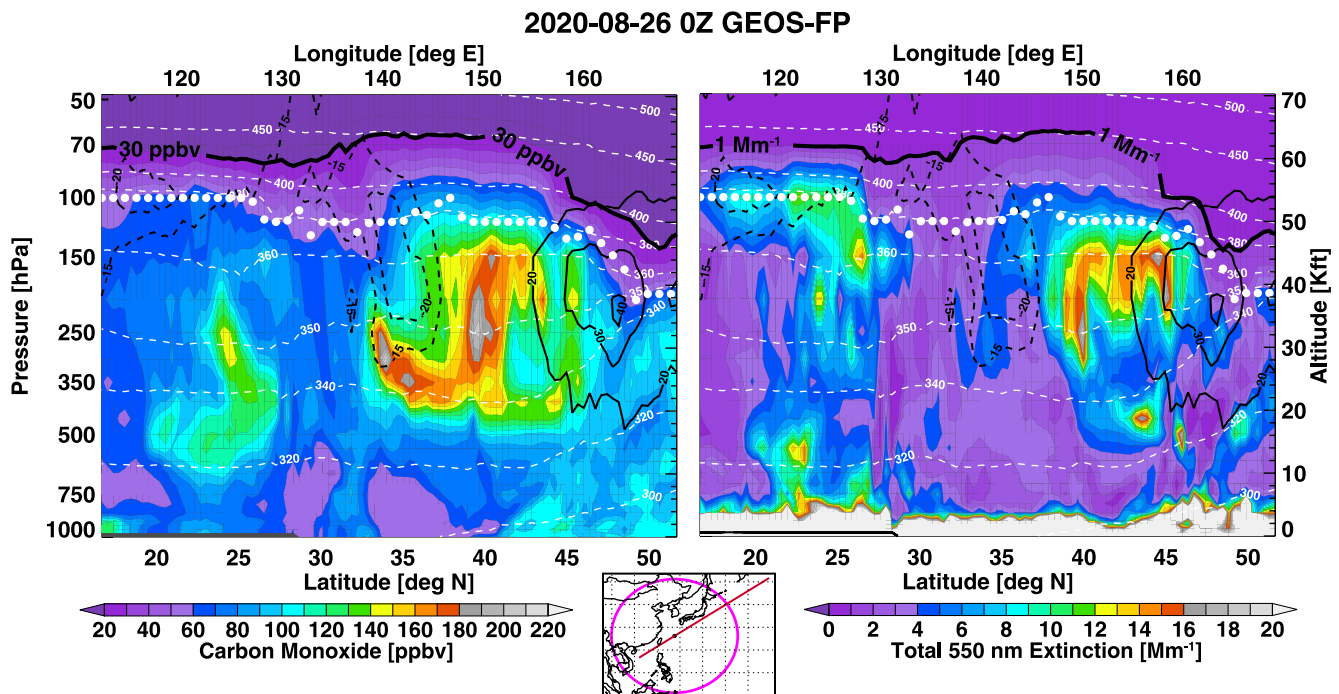


**Figure 7.** Examples of enhanced aerosol mass and number concentration in the shedding air mass from Whole Atmosphere Community Climate Model (WACCM) and Goddard Earth Observing System Forward Processing (GEOS-FP; top and bottom rows, respectively) at 100 hPa on 27 August 2020 (BC, black carbon; NO<sub>3</sub>, nitrate; SO<sub>4</sub>, sulfate; SOA, secondary organic aerosol; ACC, Aerosol number concentration in Accumulation Mode). Selected geopotential height (GPH) contours (16,690, 16,730, and 16,770 m), at 100 hPa are overlaid to indicate the anticyclone shedding.

transport (e.g., Bergman et al., 2013; Lau et al., 2018; Lee et al., 2021; Vogel et al., 2015). The “mushroom” structure clearly supports the previous analysis that, although enhanced UT CO is found to span a large longitudinal range from the Mediterranean to the Western Pacific, the BL source region is dominated by the 70°–120°E segment along the monsoon trough.



**Figure 8.** Seasonal-average CO longitude–height cross section over the Asian summer monsoon (ASM) region from the Goddard Earth Observing System Forward Processing (GEOS-FP) model. The average is over 20°–40°N latitude band, from 3 hourly model output between 15 July and 31 August 2020. Additional dynamical fields shown are potential temperature (thin dashed lines), tropopause (black dots), and meridional winds. The thick solid line marked “30 ppbv max” shows the highest altitude where the model has 30 ppbv of CO.



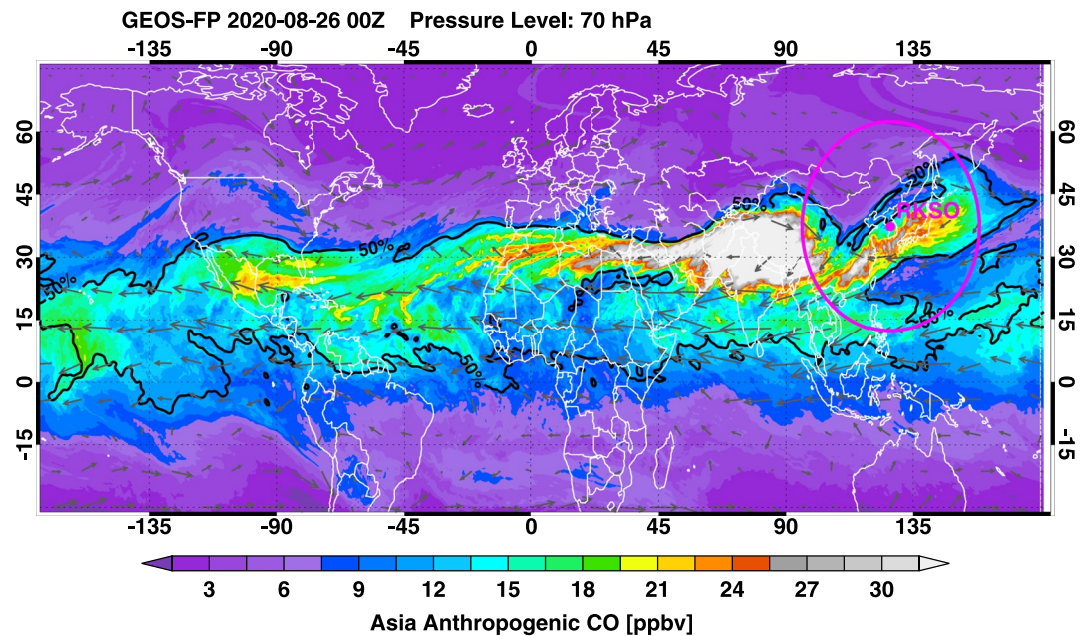
**Figure 9.** Vertical structure of Goddard Earth Observing System Forward Processing (GEOS-FP) CO (left) and total 550 nm aerosol extinction (right) during the shedding event on 26 August 2020. The location of the southwest to northeast (SWNE) cross section is marked on the locator map. Both quantities indicate a shedding signature in the region of 35°–45°N (with no sign of local vertical transport). White dots mark the tropopause height. White dashed lines show selected isentropes. Contour levels of 30 ppbv CO and 1 Mm<sup>-1</sup> aerosol extinction at 550 nm are marked by thick black lines to indicate the top of significant tropospheric transport influence.

The top of the “mushroom” is approximately aligned with the average tropopause height. Its longitudinal extent is well marked by the edge of the anticyclone, indicated by the maximum southerly and northerly meridional wind near 30° and 160°E, respectively. The “cap” part of the “mushroom” structure is slightly inclined. The center of the “cap,” represented by the layer of high CO concentration (>100 ppbv), is around 150 hPa on the west side and lowered to about 250 hPa on the east side. This structure provides direct information on the modeled convective outflow layer. The area of highest UT CO average (>110 ppbv) is shown to be near 80°E and 150 hPa, between 360 and 370 K potential temperature. This is consistent with the convective transport in the region inferred from StratoClim CO measurements (von Hobe et al., 2021). Overall, this structure indicates that the quasi-horizontal east-west transport at the top of convection is not symmetric in altitude. The westward transport is typically at a higher isentrope than that to the east. This asymmetry is consistent with the different core levels of the easterly and westerly jets (e.g., Santee et al., 2017, and references therein).

Using CO as a transport tracer, Figure 8 shows the chemical signature of the transport above the tropopause. Since the background CO concentration in the LS is typically under 20 ppbv (Herman et al., 1999; von Hobe et al., 2021) and the lifetime of CO is relatively short (1–2 months), air masses with 30 ppbv or more CO are considered to include “fresh” transport of tropospheric air. The maximum level of occurrence of the 30 ppbv CO mixing ratio is marked in Figure 8 and is shown to be near 70 hPa.

We further examine the vertical structure from GEOS-FP using a snapshot during a shedding event in Figure 9 with a southwest to northeast (SWNE) cross section of CO and 550 nm aerosol extinction. The cross section transects the “core” region of the eddy shedding air mass on 26 August 2020. Both CO and aerosol extinction show elevated values in two segments of latitude. The one in midlatitudes (35°–45°N) is associated with the shedding event, with relatively high values of both CO (>100 ppbv) and aerosol extinction (>8 Mm<sup>-1</sup>) spanning between 500 hPa and the tropopause, albeit with different structures within that layer. The other segment in lower latitudes (20°–27°N) appears to be associated with both local convection and long-range transport; however, it shows distinctive differences in vertical structure between CO and aerosol. The top of CO transport in the shedding segment (defined by mixing ratios >30 ppbv) is near 70 hPa. Similarly, the top of aerosol transport is also





**Figure 10.** Goddard Earth Observing System Forward Processing (GEOS-FP) model tagged Asia anthropogenic CO at 70 hPa. The horizontal wind field is overlaid on the map (gray arrows). The black contour labeled 50% indicates that the tagged CO within the contour is 50% or more of the total CO.

near 70 hPa (defined by  $1 \text{ Mm}^{-1}$ ). The dissimilar vertical structure between CO and aerosol extinction can be attributed to the differences in their source locations (e.g., aerosol has a significant contribution from local natural sources), source type (e.g., most CO is from direct emission, but a majority of aerosol is chemically produced in the atmosphere), and removal mechanism (e.g., aerosol is removed by dry and wet deposition, but CO is removed by reaction with OH). The example in Figure 9 suggests that although we expect broad collocation of enhanced CO and aerosols, we do not expect the two species to correlate quantitatively, because of the different relationships they have with various atmospheric processes.

Figure 10 gives a global perspective of the freshly transported ASM BL air at 70 hPa, represented by tagged CO of Asian Anthropogenic emission (Bian et al., 2013, Figure 1a) from GEOS-FP. This tagged CO map highlights the ASM transport hot spot above the region of the monsoon trough, as well as eastward shedding into the Western Pacific. The CO distribution together with the wind field also indicates the large influence of westward eddy shedding and the propagation of the ASM transported air mass along the tropical easterly jet at the 70 hPa level.

Note that the chemical signature of ASM transport deep into the stratosphere has been shown from satellite data. The chemical signature in the “tropical pipe” from ACE HCN, a long-lived biomass burning tracer, is a well-known example (Randel et al., 2010). The chemical distributions from MLS data up to the 410 K potential temperature level showed signatures from species with a range of lifetimes (e.g., Santee et al., 2017). These satellite-based chemical analyses, however, typically require averaging over monthly or seasonal time scales. The model snapshots of the chemical distribution with the flow pattern provide more insight into the transport processes on subseasonal scales.

The CO vertical structure (Figure 8) and the tagged Asian CO at 70 hPa (Figure 10) highlight the role of the ASM as a rapid transport pathway for Asian BL emissions, including halogenated VSLS, to reach stratosphere. VSLS have been found to make an important contribution to stratospheric halogen loading and thus polar ozone destruction (World Meteorological Organization [WMO], 2018). Airborne in situ measurements in the ASM convective transport region during the StratoClim campaign found much higher than the previously estimated background concentrations (by  $\sim$  a factor of 2) of Chlorinated VSLS at the tropopause level (Adcock et al., 2021), providing observational evidence that the ASM is an important source region for halogenated VSLS (Engel et al., 2018). The contribution of ASM transport to stratospheric ozone chemistry is an important motivation for characterizing this transport pathway in ACCLIP.

Since we have only shown the GEOS-FP model results in this section on vertical structure, it is important to note that vertical transport of trace gases and aerosols from the three chemical forecast models may have significant differences, due to the model resolutions, both horizontally and vertically, and the model convective transport schemes. To provide a perspective, we show in Figure S3 in Supporting Information S1 snapshots of the SO<sub>2</sub> distribution at 150 hPa and a SWNE cross section from each of the three chemistry models.

## 6. Summary and Concluding Remarks

Using a suite of models, we have provided a first comprehensive chemical and transport description of the ASM UTLS transport over the Western Pacific via eastward eddy shedding. The main objective of this study is to set the stage for an airborne investigation. The multimodel results highlight the motivation and feasibility of this investigation, as well as a set of hypotheses to be verified by the campaign. Furthermore, the study integrates and connects a number of relevant pieces of information on Asian monsoon circulation and transport from previous studies, and it provides a chemical composition-based large-scale circulation structure of the ASM system. The key findings are summarized below.

Foremost, the multimodel study further establishes most key hypotheses of ACCLIP. The resulting hypotheses and some new insights for the campaign are summarized below:

1. The chemical composition (including both gas-phase species and aerosols) of the ASM UTLS anticyclone can be sampled from the Western Pacific, owing to the rapid transport from the Tibetan anticyclone to the WPA via eastward eddy shedding at the top of convection.
2. The shedding events create a large-scale dynamical structure in the UT with “bulging” tropopause height, low-PV air in the UT, and the presence of the WPA. Associated with the dynamical structure are chemical signatures, including the enhancement of BL transport tracers, such as CO and aerosols. The models are consistent in their capability of forecasting the location of the shedding air masses for the airborne sampling.
3. The shedding events are expected to transport a wide spectrum of trace gas species and elevated aerosol loading with increased organic carbon (SOA), NO<sub>3</sub>, and sulfate concentrations that are clearly distinguished from background aerosols in the UT and the LS.
4. The shedding events represent a key mechanism by which ASM convectively transported air masses exit the confinement of the anticyclone and thus alter the composition of LS air, bringing the influence of “freshly” transported Asian BL air up to 70 hPa globally. This rapid transport pathway is of special interest for stratospheric ozone chemistry and the impact of halogenated VSLS from Asian emissions.
5. Although the models show broad consistency in predicting shedding locations, there is a significant spread in models’ predicted amount of BL species transport and aerosol formation in the UTLS. The in situ measurements from ACCLIP are expected to provide significant new information for reducing the models’ uncertainties.

In addition to updating these hypotheses, an overall picture of the large-scale ASM circulation and transport emerges from this study that brought together the research and understanding of the ASM from monsoon dynamics studies and the composition transport studies. Specifically:

6. The back trajectory diagnostic of transport origins using ERA5 wind fields (Figure 2) identifies that the air masses in the ASM anticyclone shedding left the Asian BL primarily in the region between the monsoon trough and the Tibetan Plateau.

As a key element of the monsoon system, the monsoon trough, links the moisture brought by the low-level jet to deep monsoon convection and heavy rainfall (e.g., Ding & Sikka, 2006; Krishnamurti & Bhalme, 1976). Together with the Tibetan Plateau heating, the region of ~30°N and ~90°E is the climatological center of the Tibetan anticyclone in the ASM season. The strong ascent in this region forms the rising branch of the monsoon Hadley cell (e.g., Yanai & Wu, 2006). The new result in Figure 2, therefore, makes a connection between air mass transport and the dynamical structure of the monsoon. Since the monsoon trough forms a part of the northern summer Intertropical Convergence Zone (ITCZ; e.g., Lawrence & Lelieveld, 2010), this connection helps to establish the ASM convective transport as part of the ITCZ flow pattern with the low-level convergence and upper-level divergence. The low-level convergent monsoonal flow could bring air masses from broad emission source regions spanning a large portion of the “Monsoon Asia,” which includes South, Southeast, and East Asia. An example of the monsoon low-level convergence zone is given in Pan et al. (2016, their Figure 8).

This new result, largely owing to the much-improved representation of convective transport by using the ERA5 wind fields (Smith et al., 2021), brings clarity to results of previous studies of monsoon transport, in which the region of the southern flank of the Tibetan Plateau was shown to be the main vertical transport channel (e.g., Bergman et al., 2013; Honomichl & Pan, 2020; Pan et al., 2016). This result also provides the context for previous air mass origin studies that used tagged tracers or convective clouds which were identified using geographical regions or political boundaries (e.g., Bucci et al., 2020; Park et al., 2009; Vogel et al., 2015).

7. The average CO longitude–height cross section (Figure 8), constructed using GEOS-FP output, provides a complementary view of ASM dynamics and large-scale circulation structure. The “two-stem mushroom” structure, evident in the CO seasonal (15 July to 31 August 2020) average, depicts the primary longitudinal locations of convective transport ( $\sim 70^\circ$ – $110^\circ$ E). This figure supports the understanding that convective transport resulted in the UT average CO enhancement near the center of anticyclone confinement at 150 hPa ( $\sim 14$ – $15$  km, or 360–370 K) in the region of the Tibetan anticyclone (centered  $\sim 80^\circ$ E). This characterization of convective transport is supported by the persistence of convectively pumped low-PV air around  $80^\circ$ E at 360–370 K (Garny & Randel, 2013; Popovic & Plumb, 2001). The subsequent eastward and westward eddy shedding of this “parent” anticyclone forms the large-scale pattern shown by satellite seasonal averages.

Again, these new findings from our study not only address the needs for ACCLIP campaign preparation but also provide a large-scale perspective of ASM transport from the Asian BL to the Western Pacific UTLS as a basis for characterizing its global impacts. We expect that the modeled chemical composition structure will also shed light on the overall ASM circulation structure and contribute to better characterizations of monsoon dynamics.

Finally, it is important to note that the ASM dynamics, and therefore related UTLS transport behavior, have large interannual variability. The relationships between monsoon convection, anticyclone characteristics, and climate states such as the ENSO phase, the Asian jet stream location, the QBO, and the Arctic oscillation are an area of active research (e.g., Manney et al., 2021, and references therein). The results of the 2020 model study and the 2022 field campaign need to be put into the context of these sources of large-scale interannual variability. This will be an important topic for ACCLIP postcampaign studies.

## Conflict of Interest

The authors declare no conflicts of interest relevant to this study.

## Data Availability Statement

The satellite data and model output used in this work are available in following locations:

MLS: [https://acdisc.gesdisc.eosdis.nasa.gov/data/Aura\\_MLS\\_Level2/ML2CO.005/2020/](https://acdisc.gesdisc.eosdis.nasa.gov/data/Aura_MLS_Level2/ML2CO.005/2020/)

IASI: [https://iasi.aeris-data.fr/CO\\_AC\\_SAF\\_IASI\\_A\\_data/](https://iasi.aeris-data.fr/CO_AC_SAF_IASI_A_data/)

GEOS: <https://portal.nccs.nasa.gov/datashare/gmao/geos-fp/das/Y2020/>

WACCM: [https://www.acom.ucar.edu/waccm/DATA/SPECIAL/WACCM\\_110L\\_Pan\\_et\\_al/](https://www.acom.ucar.edu/waccm/DATA/SPECIAL/WACCM_110L_Pan_et_al/)

CAMS: <https://ads.atmosphere.copernicus.eu/cdsapp#!/dataset/cams-global-atmospheric-composition-forecasts?tab=form>.

## References

- Adcock, K. E., Fraser, P. J., Hall, B. D., Langenfelds, R. L., Lee, G., Montzka, S. A., et al. (2021). Aircraft-based observations of ozone-depleting substances in the upper troposphere and lower stratosphere in and above the Asian summer monsoon. *Journal of Geophysical Research: Atmospheres*, 126, e2020JD033137. <https://doi.org/10.1029/2020JD033137>
- Aumann, H. H., Chahine, M. T., Gautier, C., Goldberg, M. D., Kalnay, E., McMillin, L. M., et al. (2003). AIRS/AMSU/HSB on the Aqua mission: Design, science objectives, data products, and processing systems. *IEEE Transactions on Geoscience and Remote Sensing*, 41(2), 253–264. <https://doi.org/10.1109/TGRS.2002.808356>
- Bacmeister, J. T., Suarez, M. J., & Robertson, F. R. (2006). Rain re-evaporation, boundary layer convection interactions, and Pacific rainfall patterns in an AGCM. *Journal of the Atmospheric Sciences*, 63(12), 3383–3403. <https://doi.org/10.1175/jas3791.1>
- Barth, M. C., Lee, J., Hodzic, A., Pfister, G., Skamarock, W. C., Worden, J., et al. (2012). Thunderstorms and upper troposphere chemistry during the early stages of the 2006 North American Monsoon. *Atmospheric Chemistry and Physics*, 12(22), 11003–11026. <https://doi.org/10.5194/acp-12-11003-2012>
- Bechtold, P., Semane, N., Lopez, P., Chaboureaud, J.-P., Beljaars, A., & Bormann, N. (2014). Representing equilibrium and nonequilibrium convection in large-scale models. *Journal of the Atmospheric Sciences*, 71(2), 734–753. <https://doi.org/10.1175/JAS-D-13-0163.1>

## Acknowledgments

This work is supported by the National Science Foundation (NSF) through its funding of the National Center for Atmospheric Research (NCAR), under cooperative agreement number 1852977. Q. Liang and P. R. Colarco acknowledge the support of NASA Modeling, Analysis, and Prediction Program. M. Chin acknowledges the support from NASA Aura Science Team project. Work at the Jet Propulsion Laboratory, California Institute of Technology, was carried out under a contract with the National Aeronautics and Space Administration (80NM0018D0004). O. B. Toon is supported by NSF Grant AGS-1853932. E. L. Atlas is supported by NSF Grant AGS-1853948 and NASA Grant NNX17AE43G. W. P. Smith is supported by NSF Grant AGS-1853929. We thank M. Barth for helpful comments on the manuscript, as well as J. Schwarz for a helpful discussion.

- Benedetti, A., Morcrette, J.-J., Boucher, O., Dethof, A., Engelen, R. J., Fisher, M., et al. (2009). The GEMS-AER team: Aerosol analysis and forecast in the European Centre for Medium-Range Weather Forecasts Integrated Forecast System: 2. Data assimilation. *Journal of Geophysical Research*, *114*, D13205. <https://doi.org/10.1029/2008JD011115>
- Bergman, J. W., Fierli, F., Jensen, E. J., Honomichl, S., & Pan, L. L. (2013). Boundary layer sources for the Asian anticyclone: Regional contributions to a vertical conduit. *Journal of Geophysical Research: Atmospheres*, *118*, 2560–2575. <https://doi.org/10.1002/jgrd.50142>
- Bian, H., Colarco, P. R., Chin, M., Chen, G., Rodriguez, J. M., Liang, Q., et al. (2013). Source attributions of pollution to the Western Arctic during the NASA ARCTAS field campaign. *Atmospheric Chemistry and Physics*, *13*(9), 4707–4721. <https://doi.org/10.5194/acp-13-4707-2013>
- Borsdorff, T., van de Brugh, J., Schneider, A., Lorente, A., Birk, M., Wagner, G., et al. (2019). Improving the TROPOMI CO data product: Update of the spectroscopic database and destripping of single orbits. *Atmospheric Measurement Techniques*, *12*(10), 5443–5455. <https://doi.org/10.5194/amt-12-5443-2019>
- Bossolasco, A., Jegou, F., Sellitto, P., Berthet, G., Kloss, C., & Legras, B. (2021). Global modeling studies of composition and decadal trends of the Asian Tropopause Aerosol Layer. *Atmospheric Chemistry and Physics*, *21*(4), 2745–2764. <https://doi.org/10.5194/acp-21-2745-2021>
- Bowman, K. P. (1993). Large-scale isentropic mixing properties of the Antarctic polar vortex from analyzed winds. *Journal of Geophysical Research*, *98*(D12), 23013–23027. <https://doi.org/10.1029/93JD02599>
- Bowman, K. P., & Carrie, G. D. (2002). The mean-meridional transport circulation of the troposphere in an idealized GCM. *Journal of the Atmospheric Sciences*, *59*(9), 1502–1514. [https://doi.org/10.1175/1520-0469\(2002\)059<1502:TMMTCO>2.0.CO;2](https://doi.org/10.1175/1520-0469(2002)059<1502:TMMTCO>2.0.CO;2)
- Brunamonti, S., Jorge, T., Oelsner, P., Hanumanthu, S., Singh, B. B., Kumar, K. R., et al. (2018). Balloon-borne measurements of temperature, water vapor, ozone and aerosol backscatter on the southern slopes of the Himalayas during StratoClim 2016–2017. *Atmospheric Chemistry and Physics*, *18*(21), 15937–15957. <https://doi.org/10.5194/acp-18-15937-2018>
- Bucci, S., Legras, B., Sellitto, P., D'Amato, F., Viciani, S., Montori, A., et al. (2020). Deep-convective influence on the upper troposphere–lower stratosphere composition in the Asian monsoon anticyclone region: 2017 StratoClim campaign results. *Atmospheric Chemistry and Physics*, *20*, 12193–12210. <https://doi.org/10.5194/acp-20-12193-2020>
- Burkholder, J. B., Sander, S. P., Abbott, J., Barker, J. R., Huie, R. E., Kolb, C. E., et al. (2015). *Chemical kinetics and photochemical data for use in atmospheric studies, evaluation no. 18* (JPL Publication 15-10). Jet Propulsion Laboratory. Retrieved from <http://jpldataeval.jpl.nasa.gov>
- Clerbaux, C., Boynard, A., Clarisse, L., George, M., Hadji-Lazarou, J., Herbin, H., et al. (2009). Monitoring of atmospheric composition using the thermal infrared IASI/MetOp sounder. *Atmospheric Chemistry and Physics*, *9*(16), 6041–6054. <https://doi.org/10.5194/acp-9-6041-2009>
- Davis, N. A., Callaghan, P., Simpson, I. R., & Tilmes, S. (2022). Specified dynamics scheme impacts on wave-mean flow dynamics, convection, and tracer transport in CESM2 (WACCM6). *Atmospheric Chemistry and Physics*, *22*(1), 197–214. <https://doi.org/10.5194/acp-22-197-2022>
- Dee, D. P., Uppala, S. M., Simmons, A. J., Berrisford, P., Poli, P., Kobayashi, S., et al. (2011). The ERA-interim reanalysis: Configuration and performance of the data assimilation system. *Quarterly Journal of the Royal Meteorological Society*, *137*(656), 553–597. <https://doi.org/10.1002/qj.828>
- Ding, Y., & Sikka, D. R. (2006). Ch. 4: Synoptic systems and weather. In B. Wang (Ed.), *The Asian monsoon*. Springer.
- Duncan, B. N., Logan, J. A., Bey, I., Megretskaya, I. A., Yantosca, R. M., Novelli, P. C., et al. (2007). Global budget of CO, 1988–1997: Source estimates and validation with a global model. *Journal of Geophysical Research*, *112*, D22301. <https://doi.org/10.1029/2007JD008459>
- Emmons, L. K., Schwantes, R. H., Orlando, J. J., Tyndall, G., Kinnison, D., Lamarque, J.-F., et al. (2020). The Chemistry Mechanism in the Community Earth System Model version 2 (CESM2). *Journal of Advances in Modeling Earth Systems*, *12*, e2019MS001882. <https://doi.org/10.1029/2019MS001882>
- Engel, A., Rigby, M., Burkholder, J. B., Fernandez, R. P., Froidevaux, L., Hall, B. D., et al. (2018). *Update on ozone-depleting substances (ODSs) and other gases of interest to the Montreal Protocol, Chapter 1 in scientific assessment of ozone depletion: 2018, Global Ozone Research and Monitoring Project* (Report No. 58). World Meteorological Organization.
- Enomoto, T. (2004). Interannual variability of the Bonin High associated with the propagation of Rossby waves along the Asian jet. *Journal of the Meteorological Society of Japan: Series II*, *82*(4), 1019–1034. <https://doi.org/10.2151/jmsj.2004.1019>
- Enomoto, T., Hoskins, B. J., & Matsuda, Y. (2003). The formation mechanism of the Bonin High in August. *Quarterly Journal of the Royal Meteorological Society*, *129*(587 Part A), 157–178. <https://doi.org/10.1256/qj.01.211>
- Flemming, J., Huijnen, V., Arteta, J., Bechtold, P., Beljaars, A., Blechschmidt, A.-M., et al. (2015). Tropospheric chemistry in the Integrated Forecasting System of ECMWF. *Geoscientific Model Development*, *8*(4), 975–1003. <https://doi.org/10.5194/gmd-8-975-2015>
- Garcia, R. R., & Richter, J. H. (2019). On the momentum budget of the quasi-biennial oscillation in the Whole Atmosphere Community Climate Model. *Journal of the Atmospheric Sciences*, *76*(1), 69–86. <https://doi.org/10.1175/JAS-D-18-0088.1>
- Garny, H., & Randel, W. J. (2013). Dynamic variability of the Asian monsoon anticyclone observed in potential vorticity and correlations with tracer distributions. *Journal of Geophysical Research: Atmospheres*, *118*, 13421–13433. <https://doi.org/10.1002/2013JD020908>
- Gelaro, R., McCarty, W., Suarez, M. J., Todling, R., Molod, A., Takacs, L., et al. (2017). The Modern-Era Retrospective analysis for Research and Applications, Version 2 (MERRA2). *Journal of Climate*, *30*(14), 5419–5454. <https://doi.org/10.1175/JCLI-D-16-0758.1>
- George, M., Clerbaux, C., Bouarar, I., Coheur, P.-F., Deeter, M. N., Edwards, D. P., et al. (2015). An examination of the long-term CO records from MOPITT and IASI: Comparison of retrieval methodology. *Atmospheric Measurement Techniques*, *8*(10), 4313–4328. <https://doi.org/10.5194/amt-8-4313-2015>
- Gettelman, A., Mills, M. J., Kinnison, D. E., Garcia, R. R., Smith, A. K., Marsh, D. R., et al. (2019). The Whole Atmosphere Community Climate Model version 6 (WACCM6). *Journal of Geophysical Research: Atmospheres*, *124*, 12380–12403. <https://doi.org/10.1029/2019JD030943>
- Goldberg, M. D., Kilcoyne, H., Cikaneck, H., & Mehta, A. (2013). Joint Polar Satellite System: The United States next generation civilian polar-orbiting environmental satellite system. *Journal of Geophysical Research: Atmospheres*, *118*, 13463–13475. <https://doi.org/10.1002/2013JD020389>
- Gottschaldt, K.-D., Schlager, H., Baumann, R., Bozem, H., Eyring, V., Hoor, P., et al. (2017). Trace gas composition in the Asian summer monsoon anticyclone: A case study based on aircraft observations and model simulations. *Atmospheric Chemistry and Physics*, *17*(9), 6091–6111. <https://doi.org/10.5194/acp-17-6091-2017>
- Granier, C., Darras, S., Denier van der Gon, H., Doubalova, J., Elguindi, N., Galle, B., et al. (2019). The Copernicus Atmosphere Monitoring Service global and regional emissions (April 2019 version). Retrieved from [https://atmosphere.copernicus.eu/sites/default/files/2019-06/cams\\_emissions\\_general\\_document\\_apr2019\\_v7.pdf](https://atmosphere.copernicus.eu/sites/default/files/2019-06/cams_emissions_general_document_apr2019_v7.pdf)
- Herman, R. L., Webster, C. R., May, R. D., Scott, D. C., Hu, H., Moyer, E. J., et al. (1999). Measurements of CO in the upper troposphere and lower stratosphere. *Chemosphere: Global Change Science*, *1*(1–3), 173–183. [https://doi.org/10.1016/S1465-9972\(99\)00008-2](https://doi.org/10.1016/S1465-9972(99)00008-2)
- Hersbach, H., Bell, B., Berrisford, P., Hirahara, S., Horanyi, A., Muñoz-Sabater, J., et al. (2020). The ERA5 global reanalysis. *Quarterly Journal of the Royal Meteorological Society*, *146*(730), 1999–2049. <https://doi.org/10.1002/qj.3803>
- Hong, S.-Y., Noh, Y., & Dudhia, J. (2006). A new vertical diffusion package with an explicit treatment of entrainment processes. *Monthly Weather Review*, *134*(9), 2318–2341. <https://doi.org/10.1175/mwr3199.1>

- Honovich, S. B., & Pan, L. L. (2020). Transport from the Asian summer monsoon anticyclone over the Western Pacific. *Journal of Geophysical Research: Atmospheres*, 125, e2019JD032094. <https://doi.org/10.1029/2019JD032094>
- Höpfner, M., Ungermann, J., Borrmann, S., Wagner, R., Spang, R., Riese, M., et al. (2019). Ammonium nitrate particles formed in upper troposphere from ground ammonia sources during Asian monsoons. *Nature Geoscience*, 12(8), 608–612. <https://doi.org/10.1038/s41561-019-0385-8>
- Inness, A., Blechschmidt, A.-M., Bouarar, I., Chabrilat, S., Crepulja, M., Engelen, R. J., et al. (2015). Data assimilation of satellite-retrieved ozone, carbon monoxide and nitrogen dioxide with ECMWF's Composition-IFS. *Atmospheric Chemistry and Physics*, 15(9), 5275–5303. <https://doi.org/10.5194/acp-15-5275-2015>
- Kaiser, J. W., Heil, A., Andreae, M. O., Benedetti, A., Chubarova, N., Jones, L., et al. (2012). Biomass burning emissions estimated with a global fire assimilation system based on observed fire radiative power. *Biogeosciences*, 9(1), 527–554. <https://doi.org/10.5194/bg-9-527-2012>
- Khalil, M. A. K., & Rasmussen, R. A. (1990). The global cycle of carbon monoxide: Trends and mass balance. *Chemosphere*, 20(1–2), 227–242. [https://doi.org/10.1016/0045-6535\(90\)90098-E](https://doi.org/10.1016/0045-6535(90)90098-E)
- Kinnison, D. E., Brasseur, G. P., Walters, S., Garcia, R. R., Sassi, F., Boville, B. A., et al. (2007). Sensitivity of chemical tracers to meteorological parameters in the MOZART-3 chemical transport model. *Journal of Geophysical Research*, 112, D20302. <https://doi.org/10.1029/2006JD007879>
- Koster, R. D., Suárez, M. J., Ducharne, A., Stieglitz, M., & Kumar, P. (2000). A catchment-based approach to modeling land surface processes in a GCM: I. Model structure. *Journal of Geophysical Research*, 105(D20), 24809–24822. <https://doi.org/10.1029/2000JD900327>
- Krishnamurti, T. N., & Bhalme, H. H. (1976). Oscillations of a monsoon system: I—Observational aspects. *Journal of the Atmospheric Sciences*, 33(10), 1937–1954. [https://doi.org/10.1175/1520-0469\(1976\)033<1937:OOAMSP>2.0.CO;2](https://doi.org/10.1175/1520-0469(1976)033<1937:OOAMSP>2.0.CO;2)
- Lamarque, J.-F., Emmons, L. K., Hess, P. G., Kinnison, D. E., Tilmes, S., Vitt, F., et al. (2012). CAM-Chem: Description and evaluation of interactive atmospheric chemistry in the Community Earth System Model. *Geoscientific Model Development*, 5(2), 369–411. <https://doi.org/10.5194/gmd-5-369-2012>
- Lau, W. K. M., Yuan, C., & Li, Z. (2018). Origin, maintenance and variability of the Asian Tropopause Aerosol Layer (ATAL): The roles of monsoon dynamics. *Scientific Reports*, 8(1), 3960. <https://doi.org/10.1038/s41598-018-22267-z>
- Lawrence, M. G., & Lelieveld, J. (2010). Atmospheric pollutant outflow from southern Asia: A review. *Atmospheric Chemistry and Physics*, 10(22), 11017–11096. <https://doi.org/10.5194/acp-10-11017-2010>
- Lee, K.-O., Barret, B., Flochmoën, E. L., Tulet, P., Bucci, S., von Hobe, M., et al. (2021). Convective uplift of pollution from the Sichuan Basin into the Asian monsoon anticyclone during the StratoClim aircraft campaign. *Atmospheric Chemistry and Physics*, 21(5), 3255–3274. <https://doi.org/10.5194/acp-21-3255-2021>
- Legras, B., & Bucci, S. (2020). Confinement of air in the Asian monsoon anticyclone and pathways of convective air to the stratosphere during the summer season. *Atmospheric Chemistry and Physics*, 20(18), 11045–11064. <https://doi.org/10.5194/acp-20-11045-2020>
- Lelieveld, J., Bourtsoukidis, E., Brühl, C., Fischer, H., Fuchs, H., Harder, H., et al. (2018). The South Asian monsoon-pollution pump and purifier. *Science*, 361(6399), 270–273. <https://doi.org/10.1126/science.aar2501>
- Li, D., Vogel, B., Müller, R., Bian, J., Günther, G., & Riese, M. (2021). Tropical cyclones reduce ozone in the tropopause region over the Western Pacific: An analysis of 18-year ozonesonde profiles. *Earth's Future*, 9, e2020EF001635. <https://doi.org/10.1029/2020EF001635>
- Li, Q., Jiang, J. H., Wu, D. L., Read, W. G., Livesey, N. J., Waters, J. W., et al. (2005). Convective outflow of South Asian pollution: A global CTM simulation compared with EOS MLS observations. *Geophysical Research Letters*, 32, L14826. <https://doi.org/10.1029/2005GL022762>
- Lin, S. (2004). A “vertically Lagrangian” finite-volume dynamical core for global models. *Monthly Weather Review*, 132(10), 2293–2307. [https://doi.org/10.1175/1520-0493\(2004\)132<2293:AVLFDC>2.0.CO;2](https://doi.org/10.1175/1520-0493(2004)132<2293:AVLFDC>2.0.CO;2)
- Liu, X., Ma, P.-L., Wang, H., Tilmes, S., Singh, B., Easter, R. C., et al. (2016). Description and evaluation of a new four-mode version of the modal aerosol module (MAM4) within version 5.3 of the Community Atmosphere Model. *Geoscientific Model Development*, 9(2), 505–522. <https://doi.org/10.5194/gmd-9-505-2016>
- Liu, Y., Hoskins, B., & Blackburn, M. (2007). Impact of Tibetan orography and heating on the summer flow over Asia. *Journal of the Meteorological Society of Japan: Series II*, 85(1), 1–19. <https://doi.org/10.2151/jmsj.85b.1>
- Livesey, N. J., Read, W. G., Wagner, P. A., Froidevaux, L., Lambert, A., Manney, G. L., et al. (2020). Version 4.2x Level 2 and 3 data quality and description document (Tech. Rep. JPL D-33509 Rev. E). Jet Propulsion Laboratory. Retrieved from <http://mfs.jpl.nasa.gov>
- Lucchesi, R. (2018). File specification for GEOS FP, GMAO Office Note No. 4 (version 1.2) (61 pp.). Retrieved from [http://gmao.gsfc.nasa.gov/pubs/office\\_notes.php](http://gmao.gsfc.nasa.gov/pubs/office_notes.php)
- Luo, J., Pan, L. L., Honovich, S. B., Bergman, J. W., Randel, W. J., Francis, G., et al. (2018). Space-time variability in UTLS chemical distribution in the Asian summer monsoon viewed by limb and nadir satellite sensors. *Atmospheric Chemistry and Physics*, 18(16), 12511–12530. <https://doi.org/10.5194/acp-18-12511-2018>
- Mahnke, C., Weigel, R., Cairo, F., Vernier, J.-P., Afchine, A., Krämer, M., et al. (2021). The Asian Tropopause Aerosol Layer within the 2017 monsoon anticyclone: Microphysical properties derived from aircraft-borne in situ measurements. *Atmospheric Chemistry and Physics*, 21(19), 15259–15282. <https://doi.org/10.5194/acp-21-15259-2021>
- Manney, G. L., Santee, M. L., Lawrence, Z. D., Wargan, K., & Schwartz, M. J. (2021). A moments view of climatology and variability of the Asian summer monsoon anticyclone. *Journal of Climate*, 34(19), 7821–7841. <https://doi.org/10.1175/jcli-d-20-0729.1>
- Mills, M. J., Richter, J. H., Tilmes, S., Kravitz, B., MacMartin, D. G., Glanville, A. A., et al. (2017). Radiative and chemical response to interactive stratospheric sulfate aerosols in fully coupled CESM1(WACCM). *Journal of Geophysical Research: Atmospheres*, 122, 13061–13078. <https://doi.org/10.1002/2017JD027006>
- Müller, S., Hoor, P., Bozem, H., Gute, E., Vogel, B., Zahn, A., et al. (2016). Impact of the Asian monsoon on the extratropical lower stratosphere: Trace gas observations during TACTS over Europe 2012. *Atmospheric Chemistry and Physics*, 16, 10573–10589. <https://doi.org/10.5194/acp-16-10573-2016>
- Neely, R. R., III & Schmidt, A. (2016). *VolcanEESM: Global volcanic sulphur dioxide (SO<sub>2</sub>) emissions database from 1850 to present—Version 1.0*. Centre for Environmental Data Analysis. <https://doi.org/10.5285/76ebdc0b-0eed-4f70-b89e-55e606bcd568>
- NOAA. (2021). The Global Forecast System (GFS). Retrieved from [https://www.emc.ncep.noaa.gov/emc/pages/numerical\\_forecast\\_systems/gfs/documentation.php](https://www.emc.ncep.noaa.gov/emc/pages/numerical_forecast_systems/gfs/documentation.php)
- Pan, L. L., Honovich, S. B., Kinnison, D. E., Abalos, M., Randel, W. J., Bergman, J. W., & Bian, J. (2016). Transport of chemical tracers from the boundary layer to stratosphere associated with the dynamics of the Asian summer monsoon. *Journal of Geophysical Research: Atmospheres*, 121, 14159–14174. <https://doi.org/10.1002/2016JD025616>
- Park, M., Randel, W. J., Emmons, L. K., Bernath, P. F., Walker, K. A., & Boone, C. D. (2008). Chemical isolation in the Asian monsoon anticyclone observed in Atmospheric Chemistry Experiment (ACE-FTS) data. *Atmospheric Chemistry and Physics*, 8(3), 757–764. <https://doi.org/10.5194/acp-8-757-2008>

- Park, M., Randel, W. J., Emmons, L. K., & Livesey, N. J. (2009). Transport pathways of carbon monoxide in the Asian summer monsoon diagnosed from Model of Ozone and Related Tracers (MOZART). *Journal of Geophysical Research*, *114*, D08303. <https://doi.org/10.1029/2008JD010621>
- Park, M., Randel, W. J., Gettelman, A., Massie, S. T., & Jiang, J. H. (2007). Transport above the Asian summer monsoon anticyclone inferred from Aura Microwave Limb Sounder tracers. *Journal of Geophysical Research*, *112*, D16309. <https://doi.org/10.1029/2006JD008294>
- Ploeger, F., Konopka, P., Walker, K., & Riese, M. (2017). Quantifying pollution transport from the Asian monsoon anticyclone into the lower stratosphere. *Atmospheric Chemistry and Physics*, *17*(11), 7055–7066. <https://doi.org/10.5194/acp-17-7055-2017>
- Popovic, J. M., & Plumb, R. A. (2001). Eddy shedding from the upper-tropospheric Asian monsoon anticyclone. *Journal of the Atmospheric Sciences*, *58*(1), 93–104. [https://doi.org/10.1175/1520-0469\(2001\)058<0093:ESFTUT>2.0.CO;2](https://doi.org/10.1175/1520-0469(2001)058<0093:ESFTUT>2.0.CO;2)
- Randel, W. J., & Park, M. (2006). Deep convective influence on the Asian summer monsoon anticyclone and associated tracer variability observed with Atmospheric Infrared Sounder (AIRS). *Journal of Geophysical Research*, *111*, D12314. <https://doi.org/10.1029/2005JD006490>
- Randel, W. J., Park, M., Emmons, L., Kinnison, D., Bernath, P., Walker, K. A., et al. (2010). Asian monsoon transport of pollution to the stratosphere. *Science*, *328*(5978), 611–613. <https://doi.org/10.1126/science.1182274>
- Rémy, S., Kipling, Z., Flemming, J., Boucher, O., Nabat, P., Michou, M., et al. (2019). Description and evaluation of the tropospheric aerosol scheme in the European Centre for Medium-Range Weather Forecasts (ECMWF) Integrated Forecasting System (IFS-AER, cycle 45R1). *Geoscientific Model Development*, *12*(11), 4627–4659. <https://doi.org/10.5194/gmd-12-4627-2019>
- Rodwell, M. J., & Hoskins, B. J. (2001). Subtropical anticyclones and summer monsoons. *Journal of Climate*, *14*(15), 3192–3211. [https://doi.org/10.1175/1520-0442\(2001\)014<3192:SAASM>2.0.CO;2](https://doi.org/10.1175/1520-0442(2001)014<3192:SAASM>2.0.CO;2)
- Santee, M. L., Manney, G. L., Livesey, N. J., Schwartz, M. J., Neu, J. L., & Read, W. G. (2017). A comprehensive overview of the climatological composition of the Asian summer monsoon anticyclone based on 10 years of Aura Microwave Limb Sounder measurements. *Journal of Geophysical Research: Atmospheres*, *122*, 5491–5514. <https://doi.org/10.1002/2016JD026408>
- Schoeberl, M. R., & Newman, P. A. (1995). A multiple-level trajectory analysis of vortex filaments. *Journal of Geophysical Research*, *100*(D12), 25801–25815. <https://doi.org/10.1029/95JD02414>
- Skamarock, W. C., Klemp, J. B., Dudhia, J., Gill, D. O., Liu, Z., Berner, J., et al. (2019). A description of the advanced research WRF model version 4.1 (No. NCAR/TN-556+STR). <https://doi.org/10.5065/1dfh-6p97>
- Smith, W. P., Pan, L. L., Honomichl, S. B., Chelpon, S. M., Ueyama, R., & Pfister, L. (2021). Diagnostics of convective transport over the Tropical Western Pacific from trajectory analyses. *Journal of Geophysical Research: Atmospheres*, *126*, e2020JD034341. <https://doi.org/10.1029/2020JD034341>
- Thomason, L. W., & Vernier, J.-P. (2013). Improved SAGE II cloud/aerosol categorization and observations of the Asian Tropopause Aerosol Layer: 1989–2005. *Atmospheric Chemistry and Physics*, *13*(9), 4605–4616. <https://doi.org/10.5194/acp-13-4605-2013>
- Tilmes, S., Hodzic, A., Emmons, L. K., Mills, M. J., Gettelman, A., Kinnison, D. E., et al. (2019). Climate forcing and trends of organic aerosols in the Community Earth System Model (CESM2). *Journal of Advances in Modeling Earth Systems*, *11*, 4323–4351. <https://doi.org/10.1029/2019MS001827>
- Ungerermann, J., Ern, M., Kaufmann, M., Müller, R., Spang, R., Ploeger, F., et al. (2016). Observations of PAN and its confinement in the Asian summer monsoon anticyclone in high spatial resolution. *Atmospheric Chemistry and Physics*, *16*(13), 8389–8403. <https://doi.org/10.5194/acp-16-8389-2016>
- Vernier, J.-P., Fairlie, T. D., Deshler, T., Venkat Ratnam, M., Gadhavi, H., Kumar, B. S., et al. (2018). BATAL: The balloon measurement campaigns of the Asian Tropopause Aerosol Layer. *Bulletin of the American Meteorological Society*, *99*(5), 955–973. <https://doi.org/10.1175/BAMS-D-17-0014.1>
- Vernier, J.-P., Fairlie, T. D., Natarajan, M., Wienhold, F. G., Bian, J., Martinsson, B. G., et al. (2015). Increase in upper tropospheric and lower stratospheric aerosol levels and its potential connection with Asian Pollution. *Journal of Geophysical Research: Atmospheres*, *120*, 1608–1619. <https://doi.org/10.1002/2014JD022372>
- Vernier, J.-P., Thomason, L. W., & Kar, J. (2011). CALIPSO detection of an Asian Tropopause Aerosol Layer. *Geophysical Research Letters*, *38*, L07804. <https://doi.org/10.1029/2010GL046614>
- Vernier, J.-P., Thomason, L. W., Pommereau, J. P., Bourassa, A., Pelon, J., Garnier, A., et al. (2011). Major influence of tropical volcanic eruptions on the stratospheric aerosol layer during the last decade. *Geophysical Research Letters*, *38*, L12807. <https://doi.org/10.1029/2011GL047563>
- Vogel, B., Günther, G., Müller, R., Groß, J.-U., Hoor, P., Krämer, M., et al. (2014). Fast transport from Southeast Asia boundary layer sources to northern Europe: Rapid uplift in typhoons and eastward eddy shedding of the Asian monsoon anticyclone. *Atmospheric Chemistry and Physics*, *14*(23), 12745–12762. <https://doi.org/10.5194/acp-14-12745-2014>
- Vogel, B., Günther, G., Müller, R., Groß, J.-U., & Riese, M. (2015). Impact of different Asian source regions on the composition of the Asian monsoon anticyclone and of the extratropical lowermost stratosphere. *Atmospheric Chemistry and Physics*, *15*(23), 13699–13716. <https://doi.org/10.5194/acp-15-13699-2015>
- Vogel, B., Müller, R., Günther, G., Spang, R., Hanumanthu, S., Li, D., et al. (2019). Lagrangian simulations of the transport of young air masses to the top of the Asian monsoon anticyclone and into the tropical pipe. *Atmospheric Chemistry and Physics*, *19*, 6007–6034. <https://doi.org/10.5194/acp-19-6007-2019>
- von Hobe, M., Ploeger, F., Konopka, P., Kloss, C., Ulanowski, A., Yushkov, V., et al. (2021). Upward transport into and within the Asian monsoon anticyclone as inferred from StratoClim trace gas observations. *Atmospheric Chemistry and Physics*, *21*, 1267–1285. <https://doi.org/10.5194/acp-21-1267-2021>
- Wang, X., Randel, W., Pan, L., Wu, Y., & Zhang, P. (2022). Transient behavior of the Asian summer monsoon anticyclone associated with eastward eddy shedding. *Journal of Geophysical Research: Atmospheres*, *127*, e2021JD036090. <https://doi.org/10.1029/2021JD036090>
- Weigel, R., Mahnke, C., Baumgartner, M., Dragoneas, A., Vogel, B., Ploeger, F., et al. (2021). In situ observation of new particle formation (NPF) in the tropical tropopause layer of the 2017 Asian monsoon anticyclone—Part 1: Summary of StratoClim results. *Atmospheric Chemistry and Physics*, *21*(15), 11689–11722. <https://doi.org/10.5194/acp-21-11689-2021>
- Weigel, R., Mahnke, C., Baumgartner, M., Krämer, M., Spichtinger, P., Spelten, N., et al. (2021). In situ observation of new particle formation (NPF) in the tropical tropopause layer of the 2017 Asian monsoon anticyclone—Part 2: NPF inside ice clouds. *Atmospheric Chemistry and Physics*, *21*(17), 13455–13481. <https://doi.org/10.5194/acp-21-13455-2021>
- Wiedinmyer, C., Akagi, S. K., Yokelson, R. J., Emmons, L. K., Al-Saadi, J. A., Orlando, J. J., & Soja, A. J. (2011). The fire INventory from NCAR (FINN): A high resolution global model to estimate the emissions from open burning. *Geoscientific Model Development*, *4*(3), 625–641. <https://doi.org/10.5194/gmd-4-625-2011>
- World Meteorological Organization (WMO). (2018). Scientific Assessment of Ozone Depletion: 2018, Global Ozone Research and Monitoring Project (Report No. 58, 588 pp.).
- Yan, R.-C., Bian, J.-C., & Fan, Q.-J. (2011). The impact of the South Asia high bimodality on the chemical composition of the upper troposphere and lower stratosphere. *Atmospheric and Oceanic Science Letters*, *4*(4), 229–234. <https://doi.org/10.1080/16742834.2011.11446928>

- Yanai, M., & Wu, G. X. (2006). Ch. 13: Effects of the Tibetan Plateau. In B. Wang (Ed.), *The Asian monsoon*. Springer.
- Yang, K., Cai, W., Huang, G., Hu, K., Ng, B., & Wang, G. (2022). Increased variability of the Western Pacific subtropical high under greenhouse warming. *Proceedings of the National Academy of Sciences of the United States of America*, *119*(23), e2120335119. <https://doi.org/10.1073/pnas.2120335119>
- Yang, Y., Li, Q., Wang, H., Bai, Z., Li, D., Wang, W., & Bian, J. (2022). Contributions of various sources to the higher-concentration center of CO<sub>2</sub> within the ASM anticyclone based on GEOS-Chem simulations. *Remote Sensing*, *14*, 3322. <https://doi.org/10.3390/rs14143322>
- Yu, P., Rosenlof, K. H., Liu, S., Telg, H., Thornberry, T. D., Rollins, A. W., et al. (2017). Efficient transport of tropospheric aerosol into the stratosphere via the Asian summer monsoon anticyclone. *Proceedings of the National Academy of Sciences of the United States of America*, *114*, 6972–6977. <https://doi.org/10.1073/pnas.1701170114>
- Zhang, J., Wu, X., Bian, J., Xia, X., Bai, Z., Liu, Y., et al. (2020). Aerosol variations in the upper troposphere and lower stratosphere over the Tibetan Plateau. *Environmental Research Letters*, *15*(9), 094068. <https://doi.org/10.1088/1748-9326/ab9b43>
- Zhang, Q., Wu, G., & Qian, Y. (2002). The bimodality of the 100 hPa South Asia high and its relationship to the climate anomaly over East Asia in summer. *Japan Journal of the Meteorological Society of Japan*, *80*(4), 733–744. <https://doi.org/10.2151/jmsj.80.733>